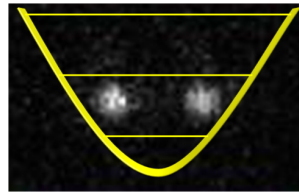




Eidgenössische Technische Hochschule Zürich
Swiss Federal Institute of Technology Zurich

Trapped
Ion
Quantum
Information



ETH Zurich, Department of Physics

HIGH FINESSE CAVITY FOR OPTICAL TRAPPING OF IONS

Master Thesis

Supervisor:

Prof. Dr. Jonathan Home

Student:

Matteo Marinelli

Spring semester 2014

Contents

1	Optical dipole trap	5
1.1	Semi-classical description	5
1.2	Quantum description	6
1.2.1	Hyperfine structure contribution	8
1.2.2	Optical trapping in a standing wave	10
1.3	Different ion species	11
1.3.1	$^{40}\text{Ca}^+$	11
1.3.2	$^9\text{Be}^+$	13
1.3.3	$^{25}\text{Mg}^+$	14
2	High Finesse Cavity	17
2.1	Theoretical description	17
2.1.1	Gaussian beams	17
2.1.2	Cavities: configurations and stability condition	18
2.1.3	Cavities: transmission and reflection	21
2.2	Optimal parameters	25
2.2.1	Beam waist	25
2.2.2	Cavity configuration and design	29
2.3	Optical Setup	32
2.4	Cavity stabilization: PDH lock	34
2.5	Effective refractive index for the mirrors	36
2.6	Experimental results	38
2.6.1	Test cavity	38
2.6.2	High finesse cavity	40
3	Fiber noise cancellation	45
3.1	Locking circuit	46
3.1.1	Results	47
4	Summary and Outlook	49
	Appendix A: Gaussian beams	53
5	Acknowledgements	55

Introduction

Quantum simulation is one of the most promising fields in quantum information science. The goal is to investigate the properties of an other quantum system in a controllable way [22]. This field of study covers a great variety of topics: from dissipation processes in a controlled environment to condensed matter physics and statistical physics. In the case of trapped ions, several methods have been proposed in the last years like long ion chains [20, 19, 22], arrays of linear Paul traps [21, 1, 3] or micro-fabricated surface electrode traps[5, 2, 4]. Another method that could be used consists of optical trapping, which uses optical confinement instead of the combination of static and radio-frequency electric fields. This method makes use of the trapping potential generated by the ion-light interaction.

The idea investigated throughout this thesis is to optically trap an ion with a far detuned laser field. In this case the optical excitation is very low and the recoil force, due to photon scattering, is negligible compared to the dipole forces. The drawback of this method is that it requires more power to get a stable optical confinement. To overcome this issue we decided to design a high finesse cavity for power build-up.

In the first chapter I will introduce the main concepts of optical dipole traps and compare the behavior of three different ion species ($^{40}\text{Ca}^+$, $^9\text{Be}^+$ and $^{25}\text{Mg}^+$). In particular it will be demonstrated that $^{25}\text{Mg}^+$ is the best candidate for optical confinement due to its level structure.

In the second chapter it will be shown the experimental realization of the high finesse cavity. For this purpose, several possible configurations will be presented and compared. Experimentally we decide to built a near concentric cavity whose finesse is $F \approx 10000$ which allow a power enhancement of $S \approx 1600$. In addition I will show the obtained experimental results.

In the third chapter I will illustrate a side project of this thesis concerning the suppression of phase noise induced by a long fiber.

1 Optical dipole trap

To better understand this method, which is widely used in the neutral atoms community [11], I will first provide a basic understanding of the trapping phenomena by exploring the mechanisms of atom-light interaction. Therefore, I will derive the equation for the trapping potential in the case of a simple two level atom and subsequently the more difficult case of a multilevel atom with fine and hyperfine structure. Once I have introduced the mathematical background I will analyze and compare three different ion species which could be used for optical trapping.

1.1 Semi-classical description

I will provide here the physics background to optical dipole traps. In particular I will analyze the interaction of the ion with a light that is far-detuned from its internal transition. As we will see, for such a case the optical excitation is very low and the recoil effect coming from photon scattering is negligible compared to the dipole force.

As a first approach let us consider the effect of a classical field onto an atom. In this frame, the field is described by an electric field \mathbf{E} which oscillates at a frequency ω : $\mathbf{E} = \mathbf{e}E(\mathbf{r})\exp(i\omega t) + c.c.$ where \mathbf{e} corresponds to the polarization of the field. Such a field will induce an atomic dipole moment \mathbf{p} which will also oscillate with frequency ω along \mathbf{e} . The amplitude of the dipole momentum is given by

$$p = \alpha E , \quad (1.1)$$

where E is the electric field amplitude and α is the complex atomic polarizability [10]. In a semiclassical approach, it is possible to calculate the complex polarizability α by considering the atom as a two level system with a transition frequency ω_0 and with a spontaneous decay rate Γ for the excited state. By solving the equations for the coupled system [10], one can derive that

$$\alpha = 6\pi\epsilon_0 c^3 \frac{\Gamma\omega_0^2}{\omega_0^2 - \omega^2 - i(\omega^3/\omega_0^2)\Gamma} , \quad (1.2)$$

where the damping rate is

$$\Gamma = \frac{\omega_0^3}{3\pi\epsilon_0\hbar c^3} |\langle e|\mu|g\rangle|^2 . \quad (1.3)$$

In this final expression the dipole matrix element between the excited state $|e\rangle$ and the ground state $|g\rangle$ plays an important role. It is important to say that the result given for α is only valid in the case of low saturation. Nevertheless, in the case we are interested in (namely the far-detuned limit), even the high intensities of the driving field will lead to very low saturation.

From these last results it is possible to define the interaction potential U as [11]

$$U(\mathbf{r}) = -\frac{1}{2}\langle \mathbf{p}\mathbf{E} \rangle = -\frac{3\pi c^2}{2\omega_0^3} \left(\frac{\Gamma}{\omega_0 - \omega} + \frac{\Gamma}{\omega_0 + \omega} \right) I(\mathbf{r}) , \quad (1.4)$$

where we consider the time average over the oscillation period and $I \propto E^2$ is the intensity of the field. Defining the absorbed power P_{abs} as

$$P_{abs} = \langle \dot{\mathbf{p}}\mathbf{E} \rangle , \quad (1.5)$$

one can retrieve the expression for the scattering rate Γ_{sc} as

$$\Gamma_{sc} = \frac{P_{abs}}{\hbar\omega} = \frac{3\pi c^2}{2\hbar\omega_0^3} \left(\frac{\omega}{\omega_0} \right)^3 \left(\frac{\Gamma}{\omega_0 - \omega} + \frac{\Gamma}{\omega_0 + \omega} \right)^2 I(\mathbf{r}) . \quad (1.6)$$

The equations for U and Γ_{sc} hold in general for every ω . Despite working in a far detuned regime, usual experiments of quantum information processing with trapped particles use frequencies ω for which the detuning, $\Delta = \omega - \omega_0$, is small compared to the resonant frequency ($\Delta/\omega_0 \ll 1$). Therefore we can neglect all the terms which rotate with a frequency $\omega + \omega_0$. This assumption is known as the *rotating-wave approximation*. In this picture, the above equations can be rewritten as [11]

$$U(\mathbf{r}) = \frac{3\pi c^2}{2\omega_0^3} \frac{\Gamma}{\Delta} I(\mathbf{r}) \quad (1.7)$$

$$\Gamma_{sc} = \frac{3\pi c^2}{2\hbar\omega_0^3} \left(\frac{\Gamma}{\Delta} \right)^2 I(\mathbf{r}) , \quad (1.8)$$

where we made the assumption of $\omega/\omega_0 \approx 1$. These two last expressions contain all the physics of the phenomena of interest.

The first thing to notice is that the scattering rate scales with a factor I/Δ^2 whereas the dipole potential scales with I/Δ . This shows that working in a far detuned limit strongly suppresses the scattering rate and thus the recoil of the atom (which is a source of heating that works against trapping). On the other side, working in this limit requires the usage of high field intensities in order to have large dipole potentials. A second thing to note is that, depending on the sign of Δ , the potential is negative either in the points with maximum intensity (red detuning, $\Delta < 0$) or in the point of minimum intensity (blue detuning, $\Delta > 0$).

1.2 Quantum description

The same result can be derived in a quantum mechanical way using the AC Stark shift [11]. This is a fundamental tool which will be used throughout the full chapter to understand which transition maintains the ion in a trapped state. The idea behind this

approach is that the effect of a far detuned light can be described as a second order perturbation in the electric field acting on the atom's levels.

Let us consider the interaction between a quantized light field and a two-level atom. The unperturbed state, where the atom is in the ground state and the field contains n photons, has an unperturbed energy of $\epsilon_1 = n\hbar\omega$. Turning on the interaction means that after sufficiently long time there will be an absorption of a photon from the atom. In such a case the energy of the system will be $\epsilon_2 = \hbar\omega_0 + (n-1)\hbar\omega = -\hbar\Delta + n\hbar\omega$.

Applying second order perturbation theory and using the interaction Hamiltonian $H_1 = -\hat{\mu}\mathbf{E}$ ($\hat{\mu}$ is the dipole matrix), the energy shift ΔE of the two levels reads

$$\Delta E = \pm \frac{|\langle e|\mu|g\rangle|^2}{\Delta} |E|^2 = \pm \frac{3\pi c^2}{2\omega_0^3} \frac{\Gamma}{\Delta} I, \quad (1.9)$$

where we used Eq.(1.3) and the plus sign is for the ground state while the minus for the excited one. The effect of the light on the atomic levels in a gaussian laser beam is shown in Fig. 1. Note that for $\Delta < 0$ (red detuning) the ground state is pulled down and therefore, for very low saturation (atom mostly in ground state), we can create a trapping potential for the ion.

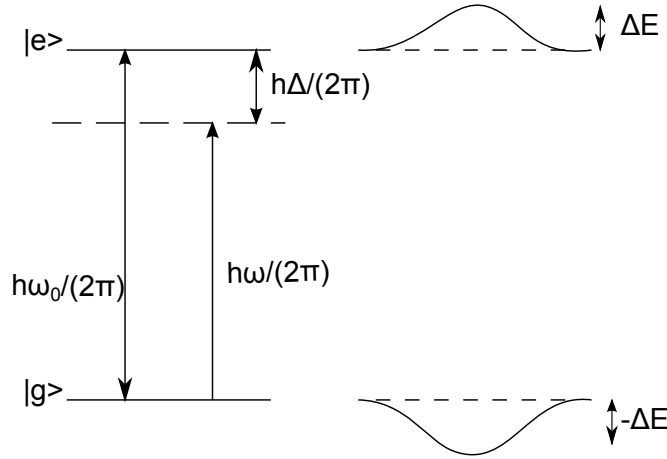


Figure 1: Left side: ground and excited state without coupling with the optical field. Right side: AC Stark shift induced by a gaussian distribution on the light field. The red detuning pushes the ground state down and the excited state up.

This approach is valid only for non degenerate levels. Usually this is not the case for atoms in zero magnetic field. Nevertheless, it can be shown that the result is still correct if there is no coupling between degenerate ground states. Thus for pure π or σ^\pm transitions this method is still applicable.

Eq. (1.9) can be generalized to a multi-level atom with transition substructure. In practice one can calculate the light shift of a particular level i just by summing all the

contributions of all the possible transitions from that level, weighted onto the transition coefficient. In a mathematical description it is possible to write the dipole matrix elements between the ground state $|g_i\rangle$ and the excited state $|e_j\rangle$ as

$$\mu_{ij} = \langle e_j | \mu | g_i \rangle = c_{ij} ||\mu|| , \quad (1.10)$$

where c_{ij} is the transition coefficient which contains the strength of the coupling between the two levels and $||\mu||$ is the reduced matrix element. With this definition in mind, one can write the energy shift of the ground state $|g_i\rangle$ as [11]

$$\Delta E_i = \frac{3\pi c^2}{2\omega_0^3} I(\mathbf{r}) \sum_j \frac{\Gamma_{ji} c_{ij}^2}{\Delta_{ij}} , \quad (1.11)$$

where the sum runs over all the states j and the contribution of each level is given by the ratio of the line strength, c_{ij}^2 , and the detuning of the transition.

1.2.1 Hyperfine structure contribution

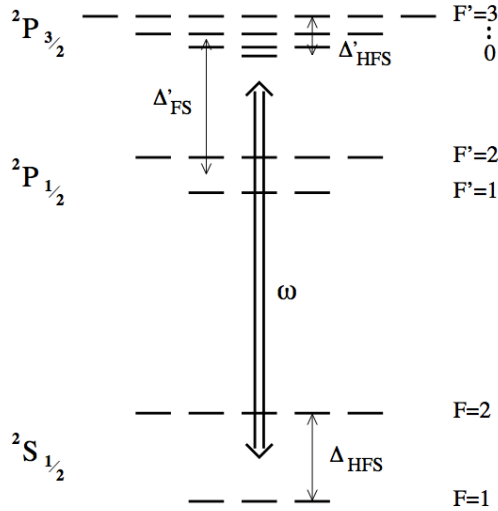


Figure 2: Example of hyperfine structure given by the coupling with a nuclear spin $I = \frac{1}{2}$ [11].

Eq.(1.11) can be generally applied for all kinds of atoms. For quantum information processing with trapped ions we are mainly interested in those of the second group like Ca^+ , Be^+ or Mg^+ , even if other elements like B^+ or Yb^+ could also be used. These elements don't have the same structure; some of them like Be^+ or Mg^+ , show also hyperfine splitting of the levels due to the coupling with the nuclear spin. Therefore, for further steps, it is worth generalizing the equations for the trapping potential taking into account this substructure [11].

A possible example is shown in Fig. 2, where one can notice the splitting of the ground state and of the two P states due to the coupling with the nuclear spin ($I = 1/2$). The full derivation I will briefly show relies on the assumption of resolved fine structure and unresolved hyperfine structure. In other words, it applies in the case of far detuned atom light interaction. This means that the fine structure splitting of the P state, Δ_{FS} , is larger than the laser detuning Δ which in turn is larger than the hyperfine splitting of the ground state Δ_{HFS} . In other words, we can restrict our description of the atom only to the fine structure levels, and thus on the transitions from the ground state $J = \frac{1}{2}$ to the excited state $J' = \frac{1}{2}, \frac{3}{2}$. In this frame, to calculate the AC Stark shift of the Zeeman sub-levels of the ground state, $m_J = \pm \frac{1}{2}$, polarization has to be taken into account [11]. In case of circular polarization the relevant line strength factors are dependent on the particular magnetic level we start from. It is possible to show that their value is $\frac{2}{3}(1 \pm m_J)$ and $\frac{1}{3}(1 \mp m_J)$ for the $J = \frac{1}{2} \rightarrow J' = \frac{1}{2}$ and $J = \frac{1}{2} \rightarrow J' = \frac{3}{2}$ transitions, respectively. This result was calculated by Cohen-Tannoudji *et al* [12] by showing that the effect of the light beam is entirely described by a fictitious magnetic field with amplitude proportional to the intensity of the light. As a consequence, this will lift the degeneracies on the magnetic sub-levels. On the contrary, in the case of linear polarization both levels get shifted by the same amount because of symmetry reasons. In fact using the fictitious field picture, it is like having a superposition of σ^+ and σ^- polarization with the same intensities and thus the fictitious field would have zero amplitude. In such a case one can show that the line strength of the transitions is equal to $\frac{2}{3}$ for the $J = \frac{1}{2} \rightarrow J' = \frac{1}{2}$ transition and $\frac{1}{3}$ for the $J = \frac{1}{2} \rightarrow J' = \frac{3}{2}$ one.

Until now we have just considered the effect on the fine structure. A question that may arise is what happens to the hyperfine states F, m_F if we turn on again the coupling with the nuclear spin. From atomic physics [13] we know that the effects of the Zeeman splitting, in low magnetic field, onto hyperfine sub-levels can be calculated by replacing $g_J m_J$ with $g_F m_F$, where the Landé g_J factor is equal to 2. This means that in the case of circularly polarized light the line strength factors become $\frac{1}{3}(2 \pm g_F m_F)$ and $\frac{1}{3}(1 \mp g_F m_F)$, while for linear polarization there is still degeneracy of m_F states.

Now that we have the coefficients for the line strengths, we can substitute them into Eq. (1.11) to get the ground state energy shift [11]:

$$U(\mathbf{r}) = \frac{\pi c^2 \Gamma}{2\omega_0^3} \left(\frac{2 + P g_F m_F}{\Delta_{2,F}} + \frac{1 - P g_F m_F}{\Delta_{1,F}} \right) I(\mathbf{r}) , \quad (1.12)$$

where P takes care of the polarization ($P = 0, \pm 1$ for linear and circular σ^\pm polarization, respectively) and $\Delta_{1,F}$ and $\Delta_{2,F}$ are the detunings of the laser light from the transitions which go from the ground state $S_{1/2}, F$ to the center of the $P_{1/2}$ and $P_{3/2}$ levels respectively.

For our purpose it is interesting to see the far detuned limit. In this case not even the fine structure is resolved; thus we can assume that $\Delta \approx (|\Delta_{1,F}|, |\Delta_{2,F}|) \ll \Delta_{FS}$, where we have introduced the detuning Δ from the center of the $P_{1/2}$ and $P_{3/2}$ state. We can

now expand the the Eq. (1.12) for the parameter Δ_{FS}/Δ , obtaining

$$U(\mathbf{r}) \cong \frac{3\pi c^3}{2\omega_0^3} \frac{\Gamma}{\Delta} \left(1 + \frac{1}{3} P g_F m_F \frac{\Delta_{FS}}{\Delta} \right) I(\mathbf{r}) . \quad (1.13)$$

Note that the first term in this expansion is the one we calculated in Eq. (1.7) where no atom structure was considered. This can be understood by thinking that the large detuning dominates and it is like considering only the $s \rightarrow p$ transition. In such a case polarization and of course hyperfine levels do not play any role.

1.2.2 Optical trapping in a standing wave

Depending on the kind of method used to confine the particles, we can identify different types of optical traps: focused beam, crossed beam and standing wave traps. A first demonstration of ion trapping with optical confinement was made using a focused beam from a fiber, see [14]. Such traps are the simplest possible and consist of focusing a gaussian beam in the trapping point. Drawbacks of this method are the sensitivity to laser frequency noise and shallow potential wells.

Our aim is to work in a far detuned limit, where we can neglect the scattering rate of the atom with the trapping field. In such a limit, the trapping potential gets shallower and thus more power is required to trap ions. Therefore our approach is to use a high finesse cavity in which it is possible to build up more power to compensate the detuning. The cavity will also reduce the linewidth of the laser and create a standing wave between the mirrors, allowing us to create 1D lattices (see next chapter).

In such a system the intensity $I(r, z)$ to be used in Eq. (1.12) is given by [6]

$$I(r, z) = \frac{8P}{\pi\omega^2(z)} \exp\left(-2\frac{r^2}{\omega^2(z)}\right) , \quad (1.14)$$

where P is the power of the gaussian beam which propagates along the z direction and r is the radial coordinate. The quantity $\omega(z)$ is called gaussian beam radius and it is defined as

$$\omega(z) = \omega_0 \sqrt{1 + \left(\frac{z}{z_R}\right)^2} , \quad (1.15)$$

in which ω_0 is called beam waist and $z_R = \pi\omega_0^2/\lambda$ is the Rayleigh length (see next chapter for details). One thing to notice is that, due to the cavity, there is more power available and, because of constructive interference, the value for U is 4 times larger than in the case of focused beam.

Around the potential minimum, where the ion is when cold, we can assume that the radial extension is small compared to the beam waist and axially small compared to the

Rayleigh length. In this region we can approximate the potential well as [11]

$$U(r, z) \approx -U \cos^2(kz) \left[1 - 2 \left(\frac{r}{\omega_0} \right)^2 - \left(\frac{z}{z_R} \right)^2 \right]. \quad (1.16)$$

In this harmonic approximation, we can identify two different trapping axes: one axial and the other radial. The curvatures of the potential well in these directions leads to two different trapping frequencies:

$$\omega_z = k \left(\frac{-2U}{m} \right)^{1/2} \quad (1.17)$$

$$\omega_r = \left(\frac{-4U}{\omega_0^2 m} \right)^{1/2}, \quad (1.18)$$

where m is the mass of the ion.

1.3 Different ion species

Until now we have just talked about the general trapping method without applying it to any practical case. In this section I would like to bring some specific examples applying the theory that we just derived in order to compare the behavior of different ion species. In particular I will focus the attention on $^{40}\text{Ca}^+$ and $^9\text{Be}^+$, which are the species that we currently trap in the TIQI group at ETH, and $^{25}\text{Mg}^+$, which is the best candidate for this task, as it will be shown.

1.3.1 $^{40}\text{Ca}^+$

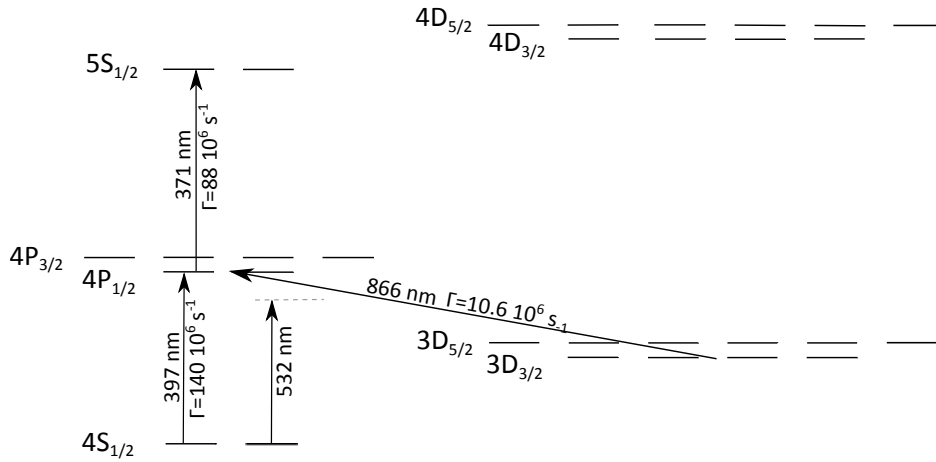


Figure 3: Level scheme of $^{40}\text{Ca}^+$ in case zero external magnetic field.

Level	Transition energy (cm^{-1})	$\Gamma(10^6s^{-1})$
$4S_{1/2} \rightarrow 4P_{1/2}$	25191.52	140
$4S_{1/2} \rightarrow 4P_{3/2}$	25414.41	147
$4P_{1/2} \rightarrow 3D_{3/2}$	11541.32	10.6
$4P_{1/2} \rightarrow 5S_{1/2}$	26975.42	88
$4P_{1/2} \rightarrow 4D_{3/2}$	31666.98	310

Table 1: Energy and line strength for the main transitions in $^{40}Ca^+$. The other transitions are not reported because they are negligible for the calculation of the trapping potential. [7]

As a first example I would like to present the case of $^{40}Ca^+$, which is currently used in our lab. Independently of the results for the trapping potential, this is the ion species we are going to use for the first tests with the optical trap. For this purpose we intend to use a Verdi laser [8] which is a solid state, diode pumped, frequency doubled, Nd:Vanadate (Nd:YVO4) laser that provides single frequency 532 nm output light. The reason is that we would like to work in a far detuned limit where the scattering rate, and thus the recoil, is negligible. Level scheme and energies are given in Fig.3 and Table 1 respectively.

Ground state: To calculate the ground state trapping depth, the main transitions to be considered are $4S_{1/2} \rightarrow 4P_{1/2}$ and $4S_{1/2} \rightarrow 4P_{3/2}$. In both cases the laser is red detuned and thus has the effect of confining the $4S$ state and anti confining the two P levels. One thing to notice is that the $S \rightarrow D$ coupling is blue detuned but since it is a quadrupole transition the line strength is so small that it does not make any difference to the ground state level shift. For a quantitative analysis one can apply Eq. (1.11) and Eq. (1.14), where we suppose to have a 532 nm light with total optical power $P \approx 1kW$ and a beam waist of $\omega_0 = 30 \mu m$. Thus, it is possible to verify that $\Delta E \simeq -2.58 \times 10^{-24} J \simeq 187 mK$, where the minus sign shows that it is a confining potential. This corresponds to trapping frequencies equal to $\omega_z \approx 2\pi \times 16.7 MHz$ and $\omega_r \approx 2\pi \times 66 kHz$.

$3D_{3/2}$ state: For Doppler cooling purposes the $4S_{1/2} \rightarrow 4P_{1/2}$ transition is used. When exciting the electron to this level the atom decays most of the time in the ground state, but with a rate of $\frac{1}{20}$ the electron falls in the $3D_{3/2}$ level. Therefore to have a stable system we would like to have all these three states confined under the effect of the optical trap. Consider now the case of $3D_{3/2}$ state: the transition which contributes most is the $3D_{3/2} \rightarrow 4P_{1/2}$. In this case, the laser light is blue detuned and thus it one can show that this leads to anti confinement for the D level and confinement for the P state. The total shift is $\Delta E = 6.15 \times 10^{-25} J$. As a result, whenever the ion fall in this state it will be lost.

$P_{1/2}$ state: The same approach can be applied for the $4P_{1/2}$ state. In this case the laser has an anti confining effect for the $4S_{1/2} \rightarrow 4P_{1/2}$ transition and a confining one for the $3D_{3/2} \rightarrow 4P_{1/2}$ coupling. Moreover this level can couple to the $5S_{1/2}$ and $4D_{3/2}$ which have a confining effect due to red detuning. Summing all these contributions together we can calculate the total shift to be $\Delta E = -5.76 \cdot 10^{-25} \text{ J} = 42 \text{ mK}$ and trapping frequencies equal to $\omega_z \approx 2\pi \times 9.5 \text{ MHz}$ and $\omega_r \approx 2\pi \times 37.8 \text{ kHz}$. Differently from the D states this level is stably trapped by the optical field.

From all this considerations we can conclude that Ca^+ is not the best choice for optical trapping. In fact it would be desirable to continuously cool the ion, but because of scattering processes when the electron jumps in the $D_{3/2}$ state the ion will be lost. Furthermore it is possible to show that also the state $D_{5/2}$ is anti confined and thus no qubit operations are possible.

1.3.2 $^9\text{Be}^+$

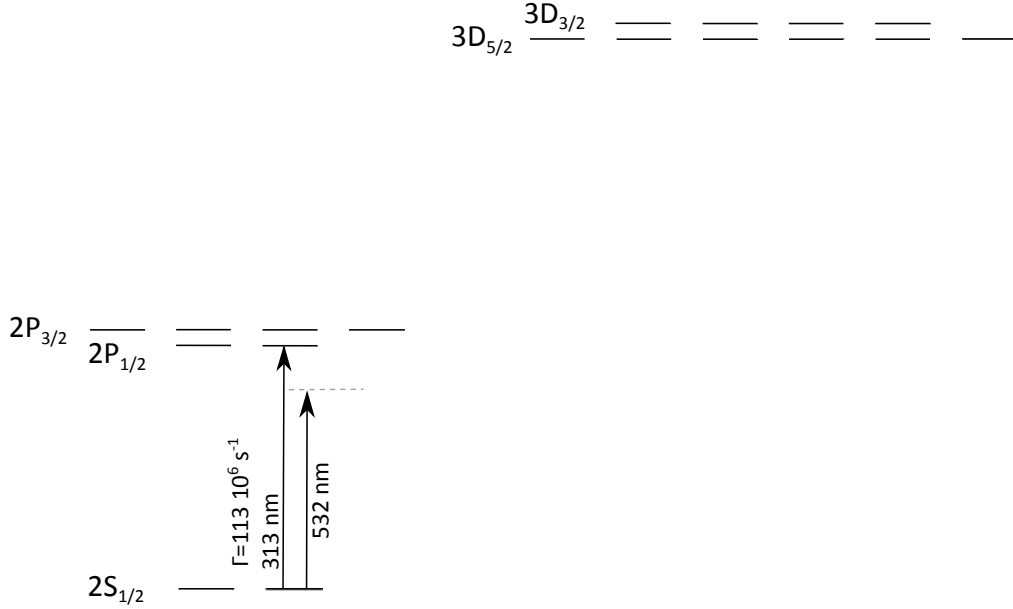


Figure 4: Level scheme of $^9\text{Be}^+$ in case of unresolved hyperfine splitting and zero external magnetic field.

The second candidate for optical trapping is $^9\text{Be}^+$ which is the other ion species we already use in the lab. Differently from Ca^+ , Be^+ shows a coupling with the nuclear spin $I = \frac{3}{2}$ which gives rise to the hyperfine splitting of the levels. For the ground state, the splitting between the the $F = 1$ and $F = 2$ is $\Delta E \approx 1.29 \text{ GHz}$ in small magnetic field.

As can be seen from the level structure in Fig. 4 and Table 2, Be^+ has of a UV transition

Level	Transition energy (cm^{-1})	$\Gamma(10^6 s^{-1})$
$2S_{1/2} \rightarrow 2P_{1/2}$	31928.74	113
$2S_{1/2} \rightarrow 2P_{3/2}$	31935.32	172
$2P_{1/2} \rightarrow 3D_{3/2}$	66125.82	1106

Table 2: Energy and line strength for the main transitions in $^9Be^+$. The other transitions are not given because negligible for the calculation of the trapping potential. [7]

from the $S_{1/2} \rightarrow P_{1/2}$ states and a more energetic one between the P and D states. Therefore we can expect qualitatively the ground state to be confined and the first excited state to be anti-confined.

This last statement can be verified by using Eq. (1.13) and Eq. (1.14), where we suppose to have a total optical power $P \approx 1kW$ and a beam waist of $\omega_0 = 30 \mu m$. In order to neglect the hyperfine structure we can consider the case of linear polarization. For such case the trapping depth of the ground state is $\Delta E = -3.82 \times 10^{-25} J = 27$ mK which corresponds to a trapping frequency of $\omega_z \approx 2\pi \times 13.7$ MHz and $\omega_r \approx 2\pi \times 54$ kHz.

Problems arise when dealing with the excited state. In fact, the AC Stark shift for the $2S_{1/2} \rightarrow 2P_{1/2}$ transition has the effect of pushing down the ground state and pushing up the P states. To have a nicely confined P level we require the total AC shift for this state to be negative. Unfortunately this is not the case because the $2P_{1/2} \rightarrow 3D_{3/2}$ transition has a very large detuning. Indeed, the total energy shift is $\Delta E = 2.47 \times 10^{-25}$ J. This means that using Be^+ could be difficult for qubit operations like state initialization and cooling mechanisms.

1.3.3 $^{25}Mg^+$

As a third example I would like to present the case of $^{25}Mg^+$. Unlike the other two ion species, Mg^+ is not yet available in our laboratory. Nevertheless for optical trapping purposes it is one of the best choices.

Before analyzing this final statement it is important to say that magnesium has a hyperfine structure due to the coupling with the nuclear spin $I = \frac{5}{2}$. Therefore the ground state is composed of a set of hyperfine levels with $F = 3$ and $F = 2$, see Fig. (5). Similarly to Be^+ , for quantum information applications the qubit is defined between two different hyperfine levels [9] which are chosen depending on the magnetic field amplitude.

To better understand why Mg^+ is the best choice for optical trapping it is worth considering its level structure, shown in Fig. (6) and Table 3.

The first important thing to note is that the $3S_{1/2} \rightarrow 3P_{3/2}$ and $3S_{1/2} \rightarrow 3P_{1/2}$ transitions are red detuned using a 532 nm laser light and thus the ground state is pushed downwards while the two excited states are pushed upwards due to the AC Stark shift. Therefore

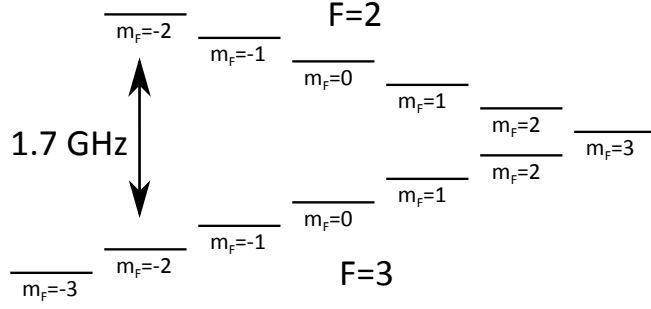


Figure 5: Hyperfine structure of the $^{25}\text{Mg}^+$ ground state. The splitting is given by the coupling with the nuclear spin $I = \frac{1}{2}$

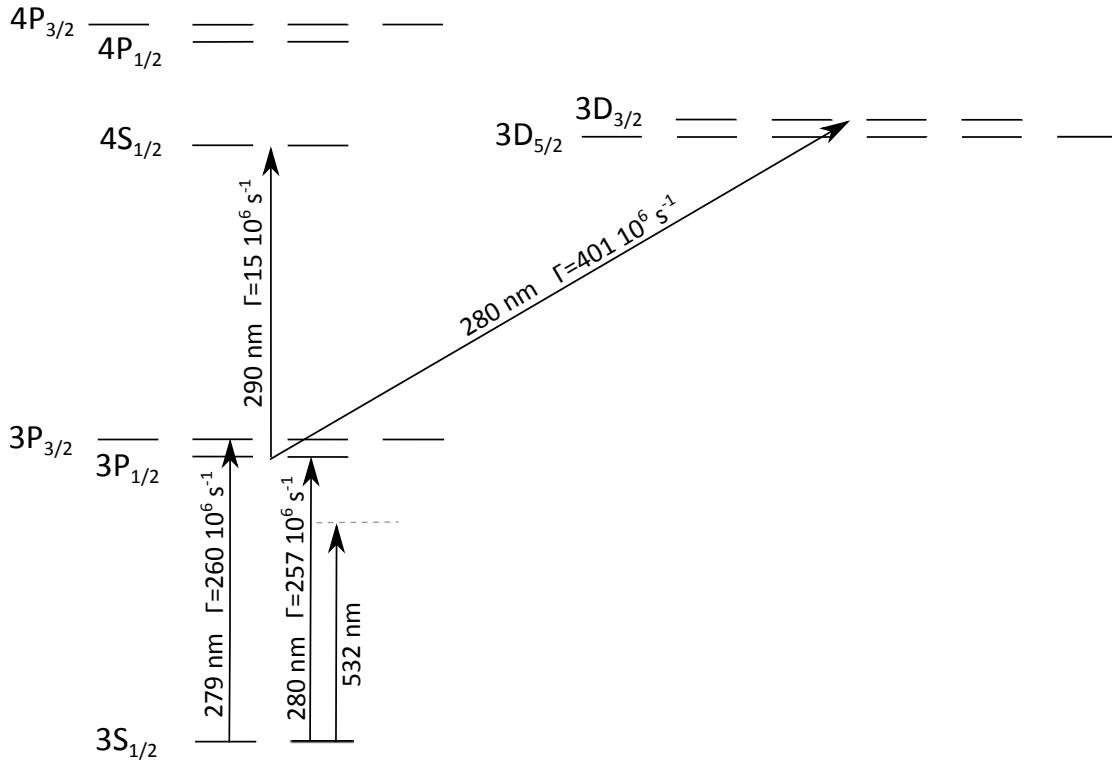


Figure 6: Energy levels in Mg^+ in the case of zero magnetic field. In this case only the fine structure is shown.

there is an anti-confining effect for the P states.

It is possible to apply Eq.(1.13) and Eq.(1.14) to calculate the trapping potential for the ground state. Note that Eq. (1.13) is dependent on the particular hyperfine level and thus will lead to different trapping potential for different magnetic levels. If the trapping frequency differences are large enough (on the order of hundreds of kHz) one can also

Level	Transition energy (cm ⁻¹)	$\Gamma(10^6\text{s}^{-1})$
$3S_{1/2} \rightarrow 3P_{1/2}$	35669.31	257
$3S_{1/2} \rightarrow 3P_{3/2}$	35760.88	260
$3P_{1/2} \rightarrow 4S_{1/2}$	34135.63	15
$3P_{1/2} \rightarrow 3D_{3/2}$	35821.75	401

Table 3: Energy and line strength for the main transitions in $^{25}\text{Mg}^+$. The other transitions are not given because negligible for the calculation of the trapping potential. [7]

think of new cooling methods or new gates schemes.

To give an idea of the confining potentials, suppose to use a total optical power of 1 kW with a waist of $30\mu\text{m}$. The trap depth for the ground state in case of linear polarization is $\Delta E = -3.33615 \times 10^{-25} \text{ J} = 0.024 \text{ K}$, which corresponds to a total trapping frequency of $\omega_z \approx 2\pi \times 7.69 \text{ MHz}$ and $\omega_r \approx 2\pi \times 30.7 \text{ kHz}$.

As already mentioned above, something interesting could happen when considering the effect of polarization on different hyperfine states. The Landé g factor for the state $F = 3$ is $g_F = \frac{1}{3}$, while for the states $F = 2$ is $g_F = -\frac{1}{3}$. Therefore we expect the largest frequency difference between the states $F = 3, m_F = 3$ and $F = 2, m_F = 2$. The axial frequency difference is $\Delta\omega_z \approx 2\pi \times 11.5 \text{ kHz}$. In order to use this feature it is necessary to be able to resolve this frequency difference using a Raman beam. Nevertheless, this value could be enhanced by increasing the power or by reducing the laser detuning.

The same calculation can be performed also for the $P_{1/2}$ state. For this purpose we do have to consider the effect of transitions from this level to the higher excited states. Indeed it is possible to see that the laser is red detuned with respect to the $3P_{1/2} \rightarrow 3D_{3/2}$ transition. Moreover, the coupling strength is double the $3S_{1/2} \rightarrow 3P_{1/2}$ transition and thus results in a confining effect also for this level. Applying the same equations used for the ground state, it turns out that the trapping potential is $\Delta E = -2.02 \times 10^{-25} \text{ J} = 0.014 \text{ K}$ which is very similar to the ground state potential depth. The corresponding trapping frequencies are $\omega_z \approx 2\pi \times 6 \text{ MHz}$ and $\omega_r \approx 2\pi \times 24 \text{ kHz}$. At this point there are two important considerations that have to be done: the first one is that unlike the case of Ca^+ and Be^+ , the relevant states are confined and thus qubit operations can be implemented. The second point is that the trapping frequencies of the ground and excited states are similar. This is of crucial importance because this fact will increase the cooling efficiency.

To conclude, we can finally state that the properties of $^{25}\text{Mg}^+$ make this ion the best candidate for optical trapping. The main disadvantage is that to perform qubit operation it is necessary to use lasers at 280 nm which require a custom laser setup [29].

2 High Finesse Cavity

As shown in the previous chapter the trapping potential is directly proportional to the optical power and inversely proportional to the detuning. Since that we would like to work in the far detuned limit, a very large amount of power is required to have a sufficiently deep potential well. Therefore the easiest way to increase laser power is to build a high finesse cavity.

To better understand the experimental techniques, in this chapter, I will first introduce the some concepts on gaussian beams and optical resonators. Later I will describe the experimental setup and characterized in the rest of this thesis.

2.1 Theoretical description

A more accurate treatment of optical beams and resonators must take into account the wave nature of light. In this section I will highlight the main properties of gaussian beams. Later I will use this notions to compare the different properties of an optical resonator.

2.1.1 Gaussian beams

A detailed derivation of gaussian beam can be found in Appendix A and in lasers textbooks [6]. For the purposes of this thesis it is worth considering the final results. In particular, the gaussian beam propagation is driven by the following equation:

$$u(x, y, z) = \frac{1}{q(z)} \exp \left[-ik \frac{x^2 + y^2}{2R(z)} - \frac{x^2 + y^2}{\omega^2(z)} \right], \quad (2.1)$$

where $R(z)$ is the radius of curvature of the beam, $\omega(z)$ is the beam radius and $q(z)$ is the complex radius defined as

$$q(z) = \frac{1}{R(z)} - i \frac{\lambda}{\pi \omega^2(z)}. \quad (2.2)$$

Note that Eq. 2.1 shows two components: the first represents a spherical wave propagating along z with real radius of curvature $R(z)$, while the represent the finite transverse amplitude variation which has a gaussian form.

An important feature of gaussian beams is that it is possible to predict the entire propagation only knowing the beam waist ω_0 (smallest transverse radius) and the wavelength of the light in the medium λ . In particular

$$\omega(z) = \omega_0 \sqrt{1 + \left(\frac{z}{z_R} \right)^2} \quad (2.3)$$

$$R(z) = z + \frac{z_R^2}{z}. \quad (2.4)$$

where z_R is called Rayleigh length and is defined by

$$z_R = \frac{\pi \omega_0^2}{\lambda} . \quad (2.5)$$

2.1.2 Cavities: configurations and stability condition

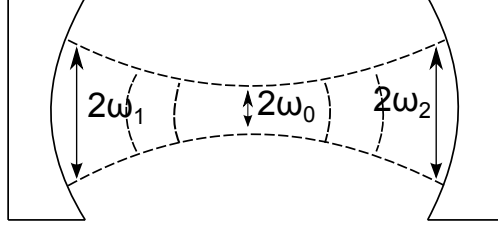


Figure 7: Picture of a simple two mirror resonator. The beam radii at the mirror surfaces ω_1, ω_2 are in general not the same.

In general, an optical cavity (in the following referred as cavity) is an apparatus which can confine a gaussian beam as a standing wave. There exist several types, but the simplest is the one created using two mirrors facing each other. A possible configuration for a gaussian resonator is shown in Fig. 7. In this example we are considering a gaussian beam with a waist ω_0 at position z_0 which is expanding in free space. For every position z the beam has a particular radius of curvature. If the radii of curvature of the two mirrors match exactly the ones of the wavefronts, each mirror will perfectly reflect the gaussian beam on itself. In this case, the system is a stable optical resonator.

There can be several configurations that one can choose to build a cavity, each of which offers different properties, see Fig. 8. Generally, the features of every configuration can be described in terms of beam waist position, length of the cavity and beam dimension. A common way of introducing those quantities is using the g factor defined as[6]

$$g = 1 - L/R . \quad (2.6)$$

As a result one can write that [6]

$$\omega_0^2 = \frac{L\lambda}{\pi} \sqrt{\frac{g_1 g_2 (1 - g_1 g_2)}{(g_1 + g_2 - 2g_1 g_2)^2}} \quad (2.7)$$

$$\omega_1^2 = \frac{L\lambda}{\pi} \sqrt{\frac{g_2}{g_1 (1 - g_1 g_2)}} \quad (2.8)$$

$$\omega_2^2 = \frac{L\lambda}{\pi} \sqrt{\frac{g_1}{g_2 (1 - g_1 g_2)}} . \quad (2.9)$$

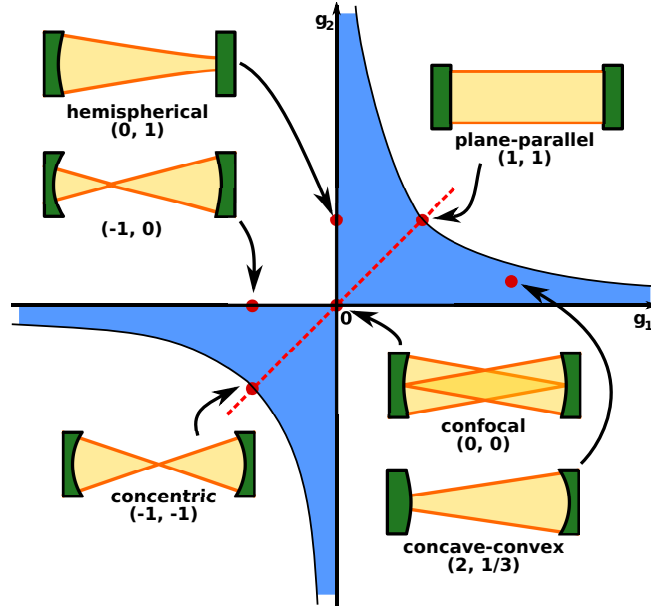


Figure 8: Stability diagram: the blue region is the stable region. Typical cavity configuration and position on the diagram are also highlighted. [15]

From these equation it is possible to see that there is a stable solution only in the case where

$$0 \leq g_1 g_2 \leq 1 . \quad (2.10)$$

Fig. 8 shows the stability diagram. Every point in this figure represents a particular configuration of the cavity.

The three different types of resonator examined during this project were the near concentric cavity, the near confocal and half symmetric resonator. In the following I will highlight their main properties.

Half symmetric resonator: This is one of the simplest and most used type of cavities. It consists of a planar mirror ($R_1 = \infty$) which is facing a curved mirror with radius of curvature $R_2 = R$. The g -factors are $g_1 = 1$ and $g_2 = g = 1 - L/R$.

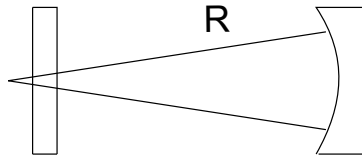


Figure 9: Half symmetric resonator. In this case the waist is on the planar mirror.

From Fig. 9 on can infer that the beam waist will be located on the surface of the planar

mirror and its dimension is given by (Eq. (2.7), Eq. (2.8))

$$\omega_0^2 = \omega_1^2 = \frac{L\lambda}{\pi} \sqrt{\frac{g}{1-g}} \quad (2.11)$$

while the spot size on the curved mirror is given by (Eq. (2.9)):

$$\omega_2^2 = \frac{L\lambda}{\pi} \sqrt{\frac{1}{g(1-g)}} . \quad (2.12)$$

The reason why such configuration is so often used is that it is easy to build and it is highly insensitive to alignment mismatches. Indeed, from Fig. 9, it is possible to note that mismatches in the vertical direction do not count at all as long as the beam waist is nicely positioned on the reflecting surface. Moreover, if the injection of the light is done normally to the flat mirror, there is no lensing effects due to curvature of surfaces or high reflective coatings.

Near concentric resonators: They are composed of two curved mirrors in which the position of the centers are close to each other, see Fig. 10.

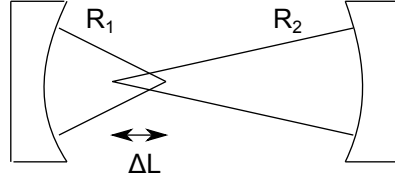


Figure 10: Near concentric resonator. The waist is located between the two centers.

For such configuration, the cavity length L is almost as large as the sum of the radii, $L = R_1 + R_2 - \Delta L$, where ΔL is small compared to R_1 and R_2 . In real experiments, mirrors with the same radius of curvature are typically used. In this case, $R = L/2 + \Delta L$ and $g_1 = g_2 = -1 + \Delta L/R$. Thanks to these definitions, in the limit of $\Delta L \ll L$, we can approximate Eq. (2.7), Eq. (2.8) and Eq. (2.9) as [6]

$$\omega_0^2 \approx \frac{L\lambda}{\pi} \sqrt{\frac{\Delta L}{4L}} \quad (2.13)$$

$$\omega_1^2 = \omega_2^2 \approx \frac{L\lambda}{\pi} \sqrt{\frac{4L}{\Delta L}} . \quad (2.14)$$

The beam waist is located in the middle of the centers and its dimension is purely determined by the distance ΔL : the shorter ΔL , the smaller the spot size at the center. Note that reducing the beam waist has the effect of increasing the beam divergence which would lead to larger spot sizes on the mirrors.

As a final remark, it is worth pointing out that this configuration is much more sensitive to misalignment. Indeed just a small tilt of one of the two mirrors would make a big change on the optical axis.

Near confocal resonators: Similarly to the case of near concentric resonators, near confocal ones are composed of two curved mirrors facing each other. The difference with the previous case is that the two focal points (located at a distance $R/2$ from the curved surface) are very close to each other and sit in the center of the system. This means that each center of curvature is placed near the the surface of the other, see Fig.11. This leads to a cavity length $L \approx R$.

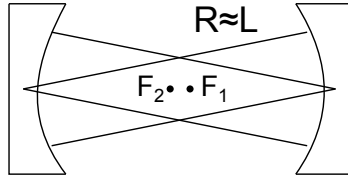


Figure 11: Symmetrical near confocal resonator. Note that the two focal point are close to each other and lies in the center of the cavity. The waist is located in the middle of the cavity.

In this limit it, is possible to rewrite Eq. (2.7), Eq. (2.8) and Eq. (2.9) as [6]

$$\omega_0^2 \approx \frac{L\lambda}{2\pi} \quad (2.15)$$

$$\omega_1^2 = \omega_2^2 \approx \frac{L\lambda}{\pi} . \quad (2.16)$$

The beam waist is never as small as in the near concentric situation and thus the beam does not diverge much. Indeed, the spot size at the center is smaller only by a factor of $1/\sqrt{2}$ compared to the beam size on the mirror surface.

The other difference with the previous case concerns stability. This kind of configuration is highly insensitive to misalignment of either mirror; a tilt in one of the two mirrors still leaves the center of curvature very close to the other mirror surface and merely displaces the optical axis by a tiny amount.

2.1.3 Cavities: transmission and reflection

Until now we have considered cavity configurations and their properties assuming a gaussian beam already present between the mirrors. In the following I assume that light is injected into the cavity from the backside of the first mirror, taking advantage of the finite transmission. Every mirror, in fact, can be characterized by two real values,

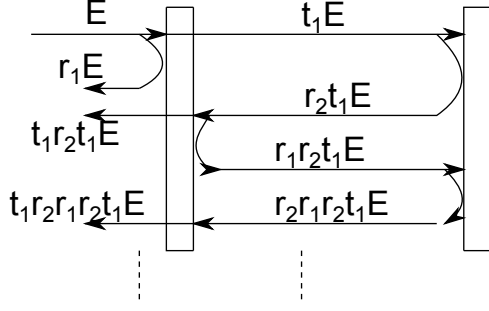


Figure 12: Cavity reflection and transmission of light.

r and t , which are the reflection and transmission coefficients. In the case of no light absorption the following relation holds:

$$r^2 + t^2 = 1 . \quad (2.17)$$

To better understand what happens to the light in the cavity consider Fig.12. The incoming electric field is $E = E_0 e^{i\omega t}$. The mirrors have reflective and transmitted coefficients r_1, t_1 and r_2, t_2 respectively. In order to calculate the total reflected field E_r , it is important to bear in mind the π phase shift of the reflection at the first mirror. The phase acquired for every round trip is

$$\Phi = 2\pi \frac{2L}{\lambda} , \quad (2.18)$$

where L is the total length of the cavity. Therefore, the total of reflected field is

$$E_r = E(-r_1 + t_1 r_2 t_1 e^{i\Phi} + t_1 r_2 r_1 r_2 t_1 e^{2i\Phi} + \dots) . \quad (2.19)$$

This sum is just a geometrical series which gives as a result [6, 16]

$$E_r = E(-r_1 + \frac{t_1^2 r_2 e^{i\Phi}}{1 - r_1 r_2 e^{i\Phi}}) . \quad (2.20)$$

The real part of this last equation drops to zero for $\Phi = n2\pi$, where n is an integer number.

This last equation can be further manipulated by introducing some quantities that are commonly used when dealing with cavities. The first one is called free spectral range (FSR) and is defined as the frequency distance between two equal modes (see next paragraph for more details on cavity modes). Mathematically we can write it as

$$FSR = \frac{c}{2L} , \quad (2.21)$$

which is also the inverse of the round trip time.

A second parameter to be introduced is the finesse F , which is a measure for the average

storage time in the cavity. The higher the finesse, the larger the power circulating into the cavity. It can be measured via the cavity ring down conversion (time needed to observe an intensity drop of $1/e$ after suddenly switching off the injection light). Therefore, the finesse depends only on the reflecting parameter r and is defined as follows:

$$F = \frac{\pi\sqrt{r_1 r_2 l}}{1 - r_1 r_2 l} , \quad (2.22)$$

where we have introduced the loss coefficient l (equal to 1 for perfect cavities). Losses in a resonator can be induced for example by scattering of light in the propagation in the medium or on the mirrors' surface.

Because of the continuous reflection of light between the mirrors, there is a power build-up in the resonator; the enhancing factor S of the cavity is defined as

$$S = \frac{t_1^2}{(1 - r_1 r_2 l)^2} . \quad (2.23)$$

The linewidth of the cavity $\Delta\nu$ is instead defined as:

$$\Delta\nu = \frac{FSR}{F} . \quad (2.24)$$

Thanks to these definitions it is possible to re-arrange Eq. (2.20). In particular it can be shown that in the case of a symmetric cavity [6, 17]

$$E_r = -Er \frac{e^{i\frac{\omega}{FSR}} - 1}{1 - r^2 e^{i\frac{\omega}{FSR}}} . \quad (2.25)$$

A possible representation of this last result is given in Fig.13. As one can see, when the frequency of the injected light is on resonance with the cavity the real part of the reflected signal goes to zero.

Cavity modes: The transverse profile of light circulating into a cavity must be an eigenfunction of the propagation equation of the light in the resonator. In a mathematical way, we can describe one round trip in a cavity using a propagation operator K . In this picture, the transverse field amplitude $E_{nm}^{(1)}$ after one round trip is [6]

$$E_{nm}^{(1)}(x, y) = \int \int K(x, y, x_0, y_0) E_{nm}^{(0)}(x_0, y_0) dx_0 dy_0 = \gamma_{nm} E_{nm}^{(0)}(x_0, y_0) , \quad (2.26)$$

where we have imposed E_{nm} to be an eigenmode with eigenvalue γ_{nm} of the round trip propagation expression.

For our experiments we only need to be able to select and lock the laser to a particular mode, typically the TEM_{00} . Thus, we only require that all the modes are non degenerate. In other words we would like the various modes to have a particular frequency which

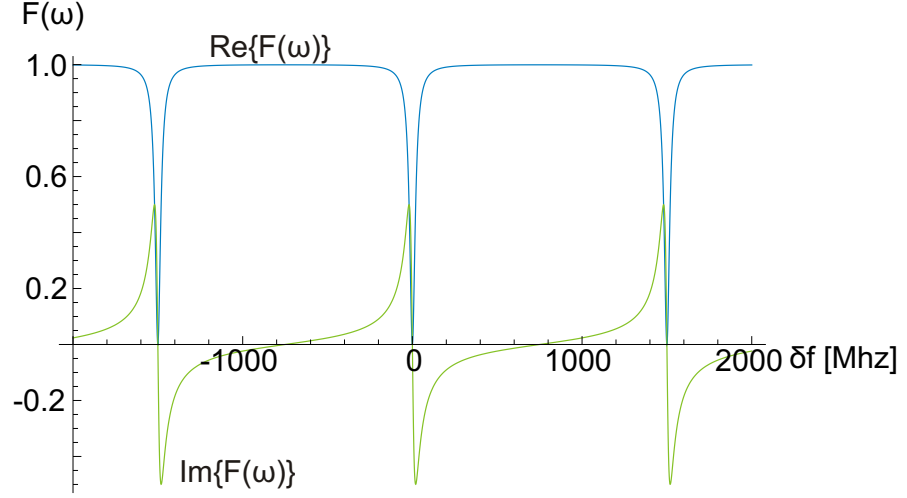


Figure 13: Real and imaginary parts of $F(\omega) = E_r/E$ where $r = 0.96$, $FSR = 1500\text{MHz}$. $\delta f = f_{\text{resonant}}\omega/2\pi$. [17]

is separated from the others at least by a cavity linewidth. For a two mirror optical resonator, the frequency separation ω_{qnm} between two different modes is [6]

$$\omega_{qnm} = \left[q + (n + m + 1) \frac{\cos^{-1}(\pm\sqrt{g_1 g_2})}{\pi} \right] \frac{2\pi c}{2L}, \quad (2.27)$$

where q is an integer number defining the axial mode, L is the cavity length and n, m define the transverse mode.

From this equation it is possible to predict the behavior of every cavity configuration. As an example we can compare the near concentric configuration and the confocal one. In particular, the term $\frac{\cos^{-1}(\pm\sqrt{g_1 g_2})}{\pi}$ goes to $1/2$ for the confocal case while it goes to 1 for the near concentric cavity. As a result the near concentric resonator shows a frequency spectrum in which all the components are well separated from each other, while the confocal one shows strong degeneracies. In this case all the even transverse modes ($n + m = \text{even number}$) are degenerate at the axial frequencies of the cavity ω_q , while the odd terms are degenerate at frequency which is exactly in the middle of the q -th and $(q + 1)$ -th axial mode.

In the end it is possible to select and maximize a particular mode by changing the angle, position and shape of the incoupled beam. The better the light is incoupled, the fewer modes that fit the cavity.

2.2 Optimal parameters

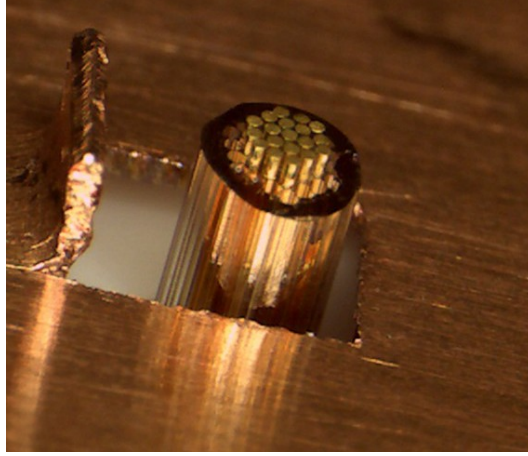


Figure 14: Image of the fiber trap used in the lab.

The aim of this project is to trap ions using the optical field generated by a high finesse cavity. $^{40}\text{Ca}^+$ and $^9\text{Be}^+$ are the two species currently used in our experiments. Therefore, as a first demonstration, we would like to use one of these two ions for optical trapping. Doppler cooling and state detection of the ion is not possible in either the cases (see Chapter 1). This means that, in order to optically trapped them it is necessary to precool them. For this purpose, we intend to use an ion trap fabricated with photonics crystal fibre technology, in the following called fiber trap, which operates with $^{40}\text{Ca}^+$.

This trap is composed of 19 gold wires of $127\text{ }\mu\text{m}$ of diameter distributed in a honeycomb structure and held together using a glass structure (see Fig. 14). The RF and ground electrodes create a potential well $90\text{ }\mu\text{m}$ above the central electrode. Doppler cooling is done using a red detuned 397 nm laser, coupling $4S_{1/2} \rightarrow 4P_{1/2}$ levels, and an 866 nm laser to re-pump from the state $3D_{3/2}$.

The final idea would be to load and Doppler cool Ca^+ with the fiber trap, switch on the optical trap and switch off for some time the fiber trap to finally detect and re-cool the ion again with the fiber trap.

2.2.1 Beam waist

The fiber trap should be placed between the cavity mirrors and $90\text{ }\mu\text{m}$ below the beam waist position. As a consequence, for an optimal loading of the optical trap, we would like to be able to move either the cavity or the fiber trap. For this application it is preferable to move the fiber trap to maintain the coupling into the cavity.

The second requirement is that the cavity field does not clip strongly on the fiber trap structure. As already mentioned above, the trap consists of gold electrodes pushed into

a glass cane: the diameter of the electrode surface is $750 \mu\text{m}$, whereas the glass cane has a diameter of $1400 \mu\text{m}$. Outside this structure, up to a distance of $2500 \mu\text{m}$, there is a copper shield that protects the electrodes from calcium deposition.

The optimal beam waist calculation is strongly dependent on the cavity configuration that we choose. Indeed, if we opt for the symmetric case, the beam waist is located exactly on the central electrode, while for a non symmetric case it will be located on one of the two cavity mirrors. Nevertheless, in both the cases, we can model the fiber trap as two knife edges placed $90\mu\text{m}$ below the beam waist position and separated by $750 \mu\text{m}$, $1400 \mu\text{m}$ or $2500 \mu\text{m}$ depending on what we would like to consider.

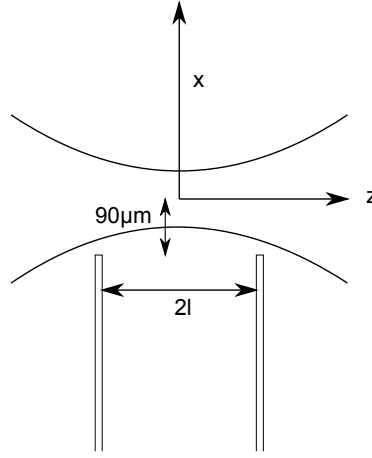


Figure 15: Fiber trap boundaries at position $z = \pm l$, where $2l = (700, 1400, 2500)\mu\text{m}$ depending if one want to use only the electrode tip, electrodes in the glass cane or the full system with the copper shield.

Symmetric case: For this system the optimal trapping position is the beam waist position which is located in the middle of the resonator. As already mentioned in the Chapter 1, the intensity profile of a gaussian beam resonating inside a cavity is[6]

$$I(x, y, z) = \frac{8P}{\pi\omega^2(z)} e^{-2(x^2+y^2)/\omega^2(z)}, \quad (2.28)$$

where we assume that $z = 0$ is the position of the beam waist. As a consequence the trap boundaries are two sharp knife edges located at $z = \pm l$ from the center and at a distance $x = -90 \mu\text{m}$ from the optical axis, see Fig. 15.

For this system, the percentage of losses as a function of the beam waist can be evaluated using the power blocked by the two sharp edges:

$$L(\omega_0, l) = 4 \frac{1}{2l} \sqrt{\frac{2}{\pi}} \left(\int_{-\infty}^{-l} dx \frac{1}{\omega(-l, \omega_0)} e^{-2x^2/\omega^2(-l, \omega_0)} + \int_{l}^{\infty} dx \frac{1}{\omega(l, \omega_0)} e^{-2x^2/\omega^2(l, \omega_0)} \right), \quad (2.29)$$

where $\omega(\pm l, \omega_0)$ is calculated using Eq. (4.13), $d = 90\mu\text{m}$ and the factor of 4 is due to the constructive interference inside the cavity.

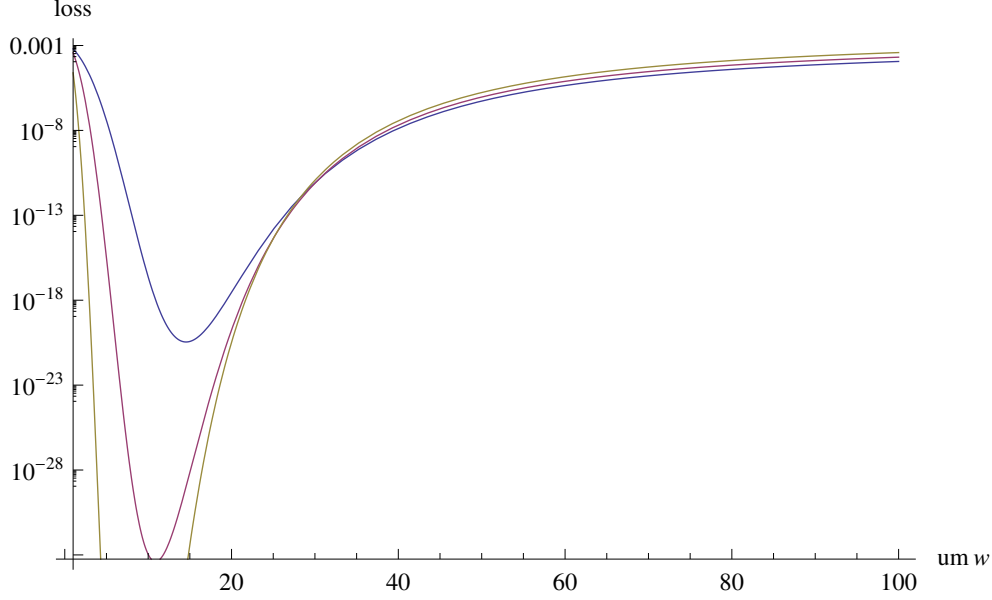


Figure 16: Plot of $L(\omega_0, l)$ as a function of the beam waist and for three different value of l . Yellow line: $l = 750 \mu\text{m}$, Red line: $l = 1400 \mu\text{m}$, Blue line: $l = 2500 \mu\text{m}$.

Fig. 16 shows the behavior of $L(\omega_0, l)$ as a function of the beam waist ω_0 and for the different value of $2l$. The percentage loss is maximal for very small value of beam waist, it reaches a minimum and it increases again reaching 1 for large value of ω_0 . This behavior can be understood by remembering that the smaller the beam waist the stronger the divergence of the gaussian beam. As a consequence both large and very small values of waist will clip the boundaries edges. The second thing that we can note is that the configuration that minimizes the losses is the one where we consider only the electrodes' tip. Nevertheless for all the three cases, the losses around the optimal beam waist are very small and negligible compared to other source of losses (imperfection of the mirror surfaces, absorption and scattering with air or dust particles, etc). Thus, we can conclude that if we decide to work with a symmetric cavity configuration we should use a beam waist which lies roughly in the range $\omega_0 \in (10, 40) \mu\text{m}$.

For this kind of symmetry a possible implementation could be a cavity composed of two curved mirrors with a reflectivity $R = 0.9998$ (value given for 532nm) with a beam waist $\omega_0 = 30\mu\text{m}$. We can also assume a total amount of losses due to external sources (dust particles scattering, imperfections, etc) of $L = 1 \times 10^{-4}$ [18] which has to be multiplied by the losses due to the clipping with the fiber trap. Moreover we assume to inject 600 mW into the cavity in order to get a circulating power of 1 kW. Form all these parameters we can calculate all the relevant quantities of the cavity (finesse, enhancing factor, potential

R	0.9998
ω	$30 \mu m$
F	10199
S	1581
P_{cavity}	950 W
$U_{trap}(4S_{1/2})$	178 mK

Table 4: List of the important parameters once given the value of R and ω . Note that ω is the spot size at the ion position. P_{cavity} is the power inside the cavity calculated by multiplying the injected power with the enhancing factor.

depth) applying Eq. (2.22), Eq. (2.23) and Eq. (1.11). In Table 4 it is possible to see the value of all these parameters using the initial conditions given before.

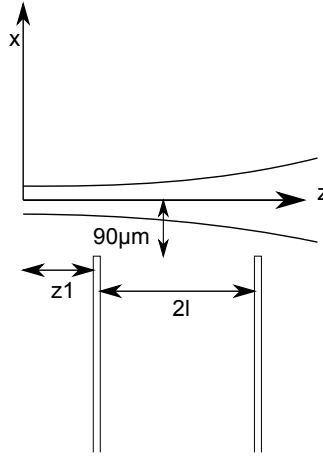


Figure 17: Fiber trap boundaries at position $z = z1$ and $z = z1 + l$. $2l = (375, 700, 1250) \mu m$ depending if one want to use only the electrode tip, electrodes in the glass cane or the full system with the copper shield.

Half symmetric case: As a second case let us analyze the half symmetric configuration for the cavity. Unlike the previous case, the beam waist is positioned on the surface of the flat mirror. This means that the spot size at the ion position will be larger than ω_0 and thus the power will be spread onto a larger surface reducing the optical intensity, see Fig. 17.

Following the same procedure introduced in the previous paragraph we can calculate the losses due to the clipping with the trap boundaries. The equation we have to integrate is exactly the same as before where the first edge is at a position $z1$ from the waist. A possible result is given in Fig. 18 where a distance of $z1 = 1 \text{ cm}$ has been chosen.

It is possible to see that there are two main difference from the symmetric case. First

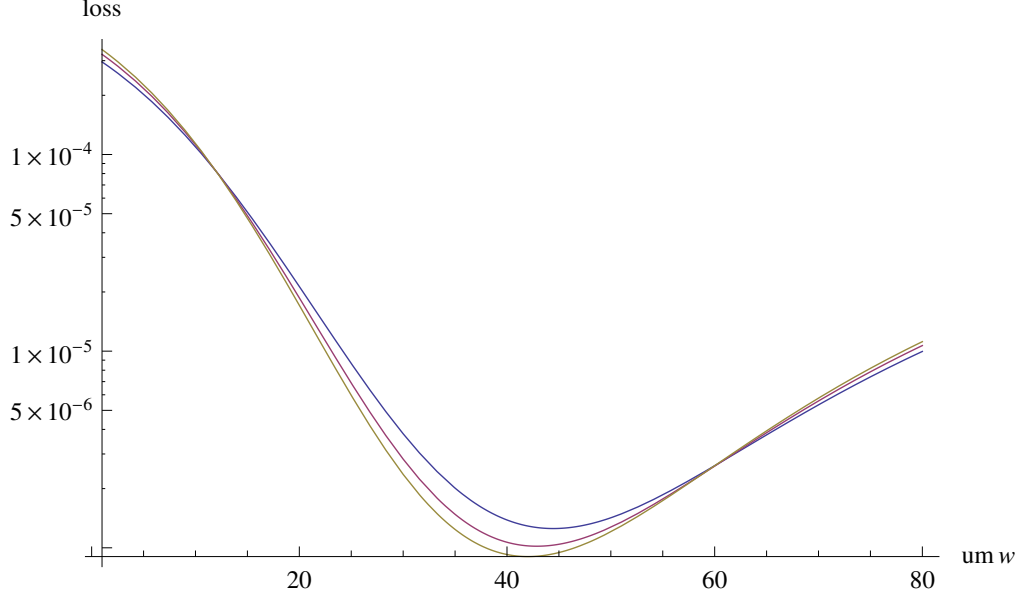


Figure 18: Plot of $L(\omega_0, l)$ as a function of the beam waist and for three different value of l . The distance z_1 is 1 cm. Yellow line: $l = 750\mu\text{m}$, Red line: $l = 1400\mu\text{m}$, Blue line: $l = 2500\mu\text{m}$.

of all, the losses and the optimal beam waist are larger in this configuration than in the symmetric one. The reason is visible in Fig. 17: the ion position is in the diverging part of the beam and thus there will be more clipping. Moreover, for geometrical reasons, we expect the optimal beam waist to increase when increasing z_1 . This means that if we want to maximize the optical trapping depth, we would like to have the flat mirror closer to the fiber trap. Unfortunately this is potentially dangerous for the system because there is the risk of creating charges on the dielectric surface of the mirror which will lead to undesired stray fields acting on the ion.

If this configuration is chosen, a possible implementation could be to use the same parameter as before where we consider a beam waist $\omega_0 = 45\mu\text{m}$ (value that minimize the losses). The result is shown in Table 5.

As one can see in this configuration the trap depth is much smaller than the symmetric configuration although the value for the finesse and the enhancing parameter are similar. What makes a big difference is the spot size on the ion which is almost doubled.

2.2.2 Cavity configuration and design

Although the half symmetric configuration is more stable than the symmetric one, the fact that the flat mirror has to be very close to the ion could lead to undesirable charging effects of the dielectric surfaces of the mirrors which will create stray fields on the

R	0.9998
ω	63 μm
F	10159
S	1568
P_{cavity}	926W
$U_{\text{trap}}(4S_{1/2})$	39 mK

Table 5: List of the important parameters once given the value of R and ω . Note that ω is the spot size at the ion position. To calculate this we considered $z_1 = 1\text{cm}$.

	R=3.8 cm	R=3 cm	R=2.5 cm
Cavity length L	7.45 cm	5.8 cm	4.76 cm
Δl distance between centers	1.5 mm	1.9 mm	2.3mm
g^2 factor (stabilty)	0.92	0.86	0.81
ω_1 spot size on mirrors	212 μm	166 μm	137 μm
FSR	2.01 GHz	2.58 GHz	3.1 GHz
linewidth $\Delta\nu$	197 kHz	253 kHz	308 kHz

Table 6: Comparison of cavity parameters for different radius of curvature. In all the three cases a beam waist of $30\mu\text{m}$ is considered.

ion. Furthermore, the trapping depth for this configuration is much smaller than the symmetric case. For these reasons we have chosen to build a symmetric resonator.

To allow a large distance from the ion and a beam waist of the order of $30\mu\text{m}$, we are left only with the near concentric configuration. The near confocal case cannot be applied because the beam waist is small only when the cavity is short, as can be seen in Eq.(2.15). This will lead to the same problems of the half symmetric resonator. The only thing that still needs to be chosen is the cavity length and thus the radius of curvature of the mirrors. In this choice we only have one constraint: the cavity should fit in the vacuum can which have an inner diameter of 10 cm. Looking at commercially available substrates, i.e. Laseroptik [23], we can choose between three possible solutions: $R = 3.8\text{ cm}$, $R = 3\text{cm}$ or $R = 2.5\text{cm}$.

In Table 6 we can see the cavity parameters for these three cases. Experimentally we decide to realize the configuration with $R = 2.5\text{ cm}$ because it is the most stable of the three. In fact, such configuration has the smallest g^2 and the largest distance between two centers. As a result a small tilt in one of the mirrors will produce a smaller effect on the optical axes.

Design: In Fig. 19 the full inventor assembly is shown. Since that it would be desirable to mechanically position the ion in the correct spot, it is important to leave enough space for moving the fiber trap and for all the cable connections. For this purpose I have designed a ring structure that can be fixed with two ends to the vacuum can. This

R	0.9998
ω	$30 \mu m$
F	10199
S	1581
P_{cavity}	950W
$U_{trap}(4S_{1/2})$	178 mK
Length L	4.76 cm
Δl distance of two centers	2.3 mm
g^2	0.81
FSR	3.1GHz
$\Delta\nu$	308 kHz

Table 7: Summary of the experimental parameters. P_{cavity} is calculated assuming 600 mW of injection.

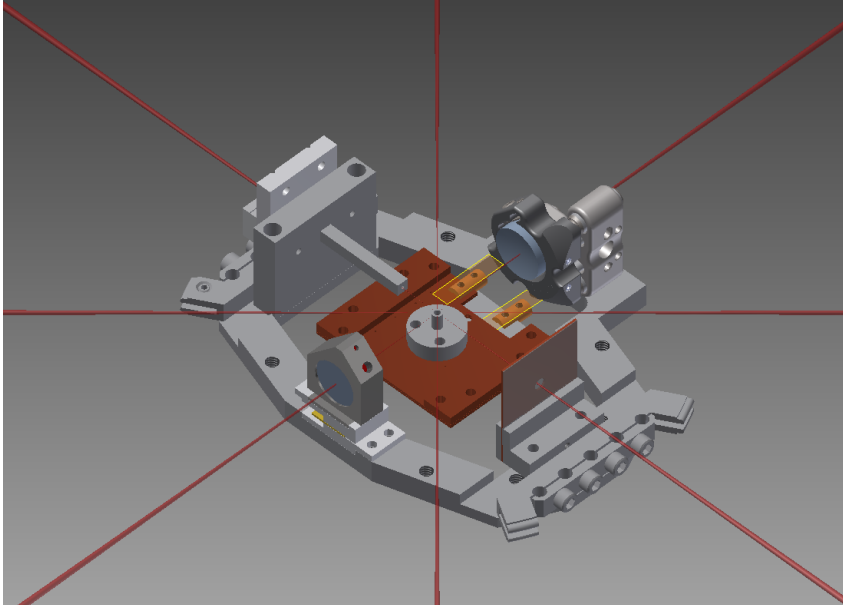


Figure 19: System assembly: in the middle it is placed the fiber trap, while the cavity mirrors are connected using a ring structure.

ring structure allows to rigidly connect the mirrors together fixing the cavity length with machine precision. In the final setup, the atom oven will not be mounted directly onto the ring structure as shown in Fig. 19 because we would like to prevent any instabilities due to heating.

One of the two mirrors is mounted on a stainless steel mount which is glued onto a shear piezo [27]. The piezo allows a fine tuning of the cavity length and can also be used to compensate slow noise, i.e vibrations or thermal fluctuations. For a fluent and fast

movement of the piezo it is important that the load is light enough and well distributed onto the surface. Fig. 20 shows the design of the mirror mount with the piezo system. The design of the fixing mechanism of the mirror was copied from the polaris mount [25]

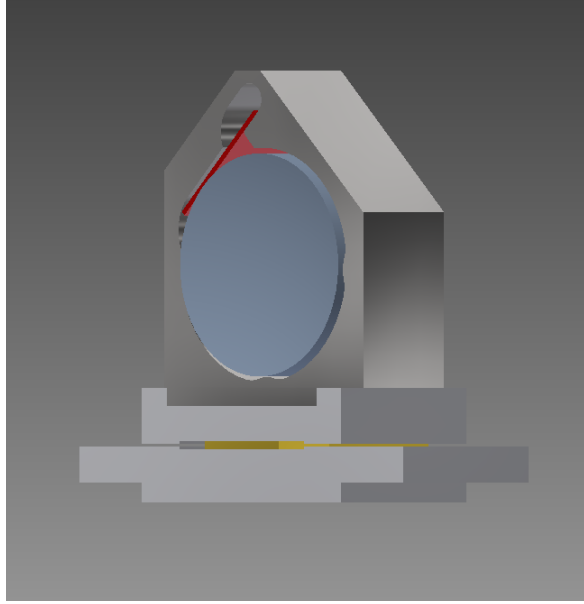


Figure 20: Mirror holder and connection with the piezo shear. In yellow is shown the piezo shear while in white the macro piece.

and it is as light as possible.

Since that the piezo works with high voltages, to avoid any charging of the holder, an insulating layer of macor is placed between the piezo and the holder. This macor piece has been machined with grooves which place the mirror holder in the exact orientation to allow movements only along the axial direction. This system is then connected to the ring holder using a second piece of macor.

On the other side, the second mirror is mounted on a Polaris mount [25] which is bakeable up to 200°C and is UHV compatible. This mount allows an accurate titling of the mirror to tune the orientation and compensate for small misalignments with the other mirror. Moreover it can also be used to adjust the cavity length and thus to compensate for small machine errors.

2.3 Optical Setup

Beside the high finesse cavity described above, during this master thesis, I also built an half symmetric resonator with low finesse. This cavity was built to test the locking electronics and to try to measure the linewidth and the fluctuations of the laser. The mirrors that we used were bought from Thorlabs [24] and their reflectivity for 532nm

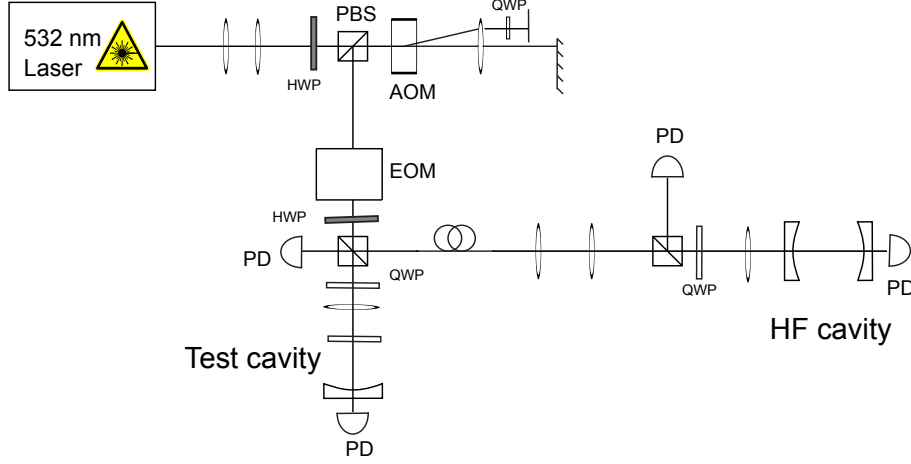


Figure 21: Optical setup.

light is $R \approx 0.996$ which corresponds to a finesse equal to $F = 783$. The total length of this cavity is 15 cm. Using Eq. (2.21) and Eq. (2.24) one can calculate a value for the free spectral range of $FSR = 1$ GHz and a linewidth of $\Delta\nu = 1.23$ MHz.

The laser that we used is a Verdi V10 [8] which is a solid state, diode pumped, frequency doubled, Nd:Vanadate (Nd:YVO4) laser that provides single frequency 532 nm output light. The output power can be set to values between 10 mW and 10 W. Experimentally it is important to note that changing the output power will also change the diameter of the output beam. In particular, in the region in which most of the work has been performed (namely from 0 to 3W), the diameter reduces while increasing the power (from 2.8 mm to 2.5 mm). In the current setup I'm using an output power of 2W which corresponds to 2.585 mm in diameter.

A second thing to state is that the laser cannot be used for any locking schemes because it does not have any component which allows active frequency tuning. Therefore, in order to control the frequency of the light going to the cavity, an acousto-optic modulator (AOM) is used (AAOpto-Electronics, model MT110-A1.5-VIS [26]). The maximal active aperture of this AOM is 1.5 mm and it has a damage threshold of $3.5\text{W}/\text{mm}^2$ at 532 nm. As visible in the data sheet the smaller the beam diameter the better the diffraction efficiency [26]. Moreover, in order to avoid a change in the beam path when modifying the driving frequency, we choose to use the double pass configuration. In such a configuration there will always be two beams inside the AOM and thus one has to take care of the damage threshold. Using the parameters specified above the maximum power we can send through the AOM is approximately 2.3 W.

Experimentally a compromise between maximal power to send into the AOM and the

diffraction efficiency was done, so we used a telescope before the AOM to reduce the optical beam diameter to 1.3 mm. With such a value the measured diffraction efficiency in the single pass is 89% and 83% in the second pass leading to a total diffraction efficiency of 74%.

After the AOM the light is sent through an electro-optic modulator (EOM) [30] which is used to create frequency sidebands on the laser that will be used for the Pound, Drever and Hall locking scheme (see next sections). To distribute light to both the cavities a polarizing beam splitter (PBS) was used and, to increase the incoupling efficiency in the high finesse cavity, we made use of an optical fiber to clean the beam profile that was distorted by the AOM.

2.4 Cavity stabilization: PDH lock

The PDH locking scheme [31] is one method of realizing a feedback loop which locks the laser frequency to the resonance frequency of a cavity. If done it properly it has the effect of reducing the laser linewidth and in the mean while stabilizing the frequency drifts to a particular cavity mode.

In principle it would be possible to measure any shift from resonance just by looking directly at the transmission or the reflection of the cavity. Nevertheless these two methods present problems which are difficult to overcome. For example when looking at cavity transmission it is impossible to distinguish between a frequency shift or just an intensity fluctuation of the light because in both the cases a reduced transmitted intensity is observed. Moreover, both in the cavity transmission and reflection, it is impossible to understand the direction of the frequency shift due to the symmetry of the peaks.

To avoid these problems Pound, Drever and Hall (PDH) proposed a scheme which makes use of the beat note between two frequency sidebands and the carrier frequency. In our setup, the sidebands are generated at the passage of a light beam through an electro-optic modulator (EOM) [17, 30]. To have an idea of the full scheme see Fig. 22. The beat note signal is read using a fast photodiode which collects the reflected light from the cavity. This RF signal is then mixed with a local oscillator also used to generate the sidebands. The output is an error signal which is sent to a PID loop that controls the AOM frequency.

A full mathematical derivation of the beat note frequency and the shape of the expected error signal can be found elsewhere [17, 32, 31]; in here I would like to jump directly to the description of the expected shape of the error signal, which is shown in Fig. 23.

A first remark is that the error signal is symmetric with respect to the central frequency and it change sign when this value is crossed. This feature allows to discriminate positive or negative frequency shifts. A second thing to note is that it is linear for frequency that are close to the carrier and the two side wings are shifted from the carrier frequency by exactly the driving frequency of the EOM.

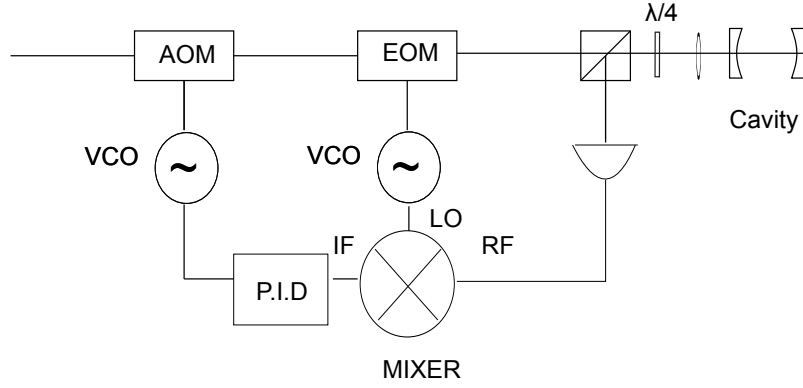


Figure 22: Schematic of setup for PDH-locking of laser to a cavity.

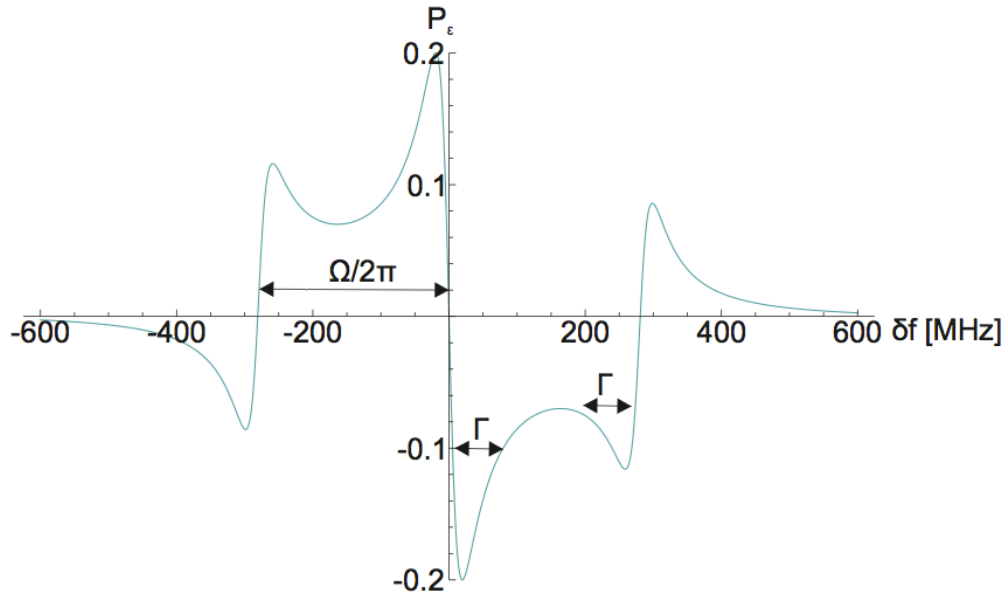


Figure 23: Example of a possible PDH signal. In this case it was evaluated for a frequency of the EOM $\Omega/2\pi = 280$ MHz and a reflectivity of the two mirrors of $r = 0.96$ [17]. $\delta f = f_{\text{resonant}} - \omega/2\pi$

As a final remark we can state that, although not so often used, measuring this signal allow to retrieve some information about the cavity; indeed the width of the small peaks/dips are exactly as large as the cavity linewidth and the well connecting the peaks become deeper by increasing the reflectivity of the mirrors.

2.5 Effective refractive index for the mirrors

To maximize the incoupling one need to match the cavity mode with the injected beam. In other words it is necessary to setup a lens configuration which focus the injected beam to have the expected beam waist position and dimension. This configuration can be predicted using ABCD matrices [6]. The matrix that describes a curved mirror is

$$M = \begin{pmatrix} 1 & 0 \\ \frac{n_1-n_2}{R} & \frac{n_1}{n_2} \end{pmatrix} \cdot \begin{pmatrix} 1 & d \\ 0 & 1 \end{pmatrix} \cdot \begin{pmatrix} 1 & 0 \\ 0 & \frac{n_1}{n_2} \end{pmatrix}, \quad (2.30)$$

where the last term represent the flat interface between air (index of refraction n_1) and mirror(index of refraction n_2); the second matrix instead represent the free space in a medium of length d while the first term is the curved interface between air and the substrate. In this, R is the radius of curvature of the surface, n_1 and n_2 are the refractive indexes of the air and the substrate respectively.

A curved mirror acts as a thick lens and thus to predict its effects one has to know its the radius of curvature and its effective refractive index of the cavity mirrors. In our case the effective refractive index of the mirror was not known; therefore, to exactly measure it, we sent a known beam through the mirror and measured the properties of the outcoming gaussian beam (beam waist dimension and position). From this fit we tuned n_2 to match the measured values.

Fig. 24 shows the measured transmitted gaussian beam and its fit for a known incoming beam. Knowing the properties of the incoming beam, it has been possible to calculate that the effective refractive index is $n = 1.27$. This value is different from the one of the fused silica substrate ($n = 1.46071$ for 532 nm light [23]). The reason is that the mirrors are coated with an AR (anti-reflection) coating on the backside and with an HR (high reflection) coating on the curved surface. For standard fused silica substrates AR coatings have a refraction index around 1.2, while HR coatings are composed of alternating layers of high refractive index (around 2.3/2.4) and low refractive index (1.2/1.3). As a result the effective refractive index of the mirror can be different from the one of the substrate.

To calculate the values shown in Fig. 24 a chopper wheel was used. The basic idea behind this method is that when the wheel cuts the beam it will be observed a drop in power. The derivative of this signal with respect to space gives the intensity profile. Since that we are dealing with gaussian beams, the beam radius can be evaluated using a gaussian fit. To have an example see Fig. 25.

Thanks to this method we were able to model our mirror and to predict the lens position that maximize the incoupling.

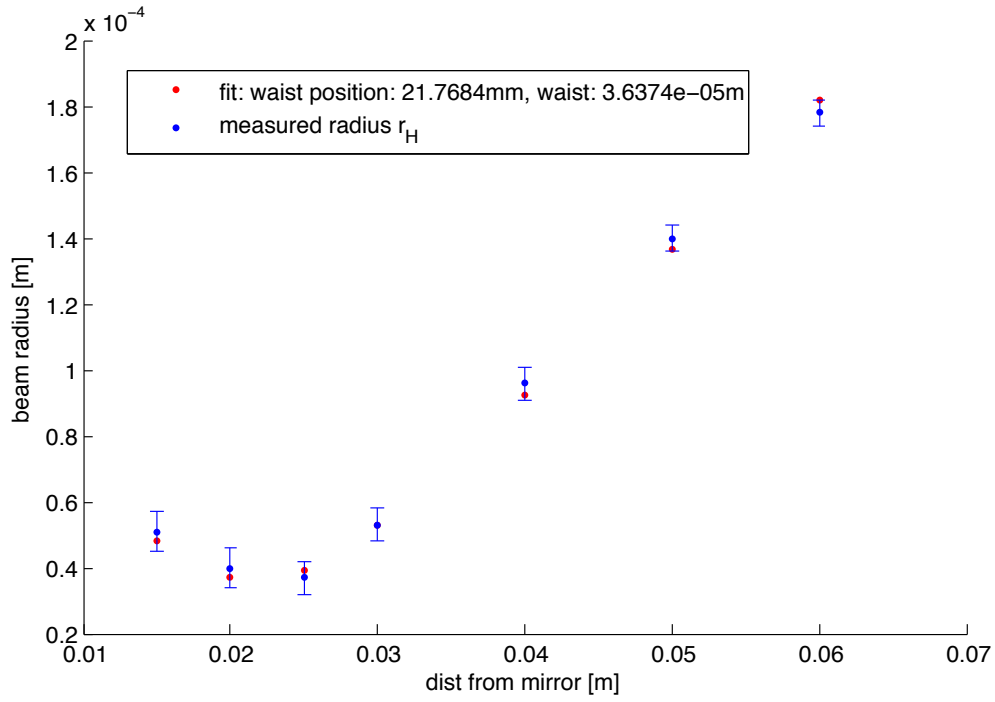


Figure 24: In red are given the measured value while in blue the fitted ones. The measure of the waist dimension was done using a chopper wheel.

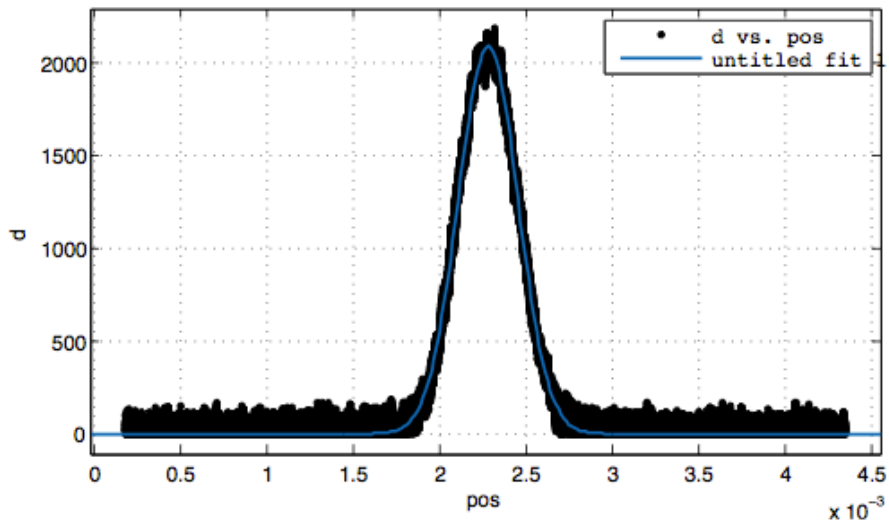


Figure 25: Gaussian fit of the measured intensity profile.

2.6 Experimental results

In this section I will present the results obtained from the test cavity concerning the locking electronics. After that I will focus on the methods used to maximize the incoupling efficiency on the high finesse cavity. Surprisingly, despite these efforts, the incoupling efficiency couldn't be increased over 3%. Therefore I will also present the analysis done to understand this behavior.

2.6.1 Test cavity

For this test cavity no particular structure was designed. In fact, the flat mirror was glued on a piezo stack [28] (to allow scanning of the cavity length), which in turn is glued on an aluminum plate and attached to a post. On the other side, the curved mirror is placed in a Polaris mirror mount and positioned on a three axis translation stage which allows to tune the position to match the resonant condition.

To test the electronics we just require to have a single mode to lock to. Fig. 26 it is shown the cavity transmission while scanning the cavity length by a full free spectral range using the piezo stack.

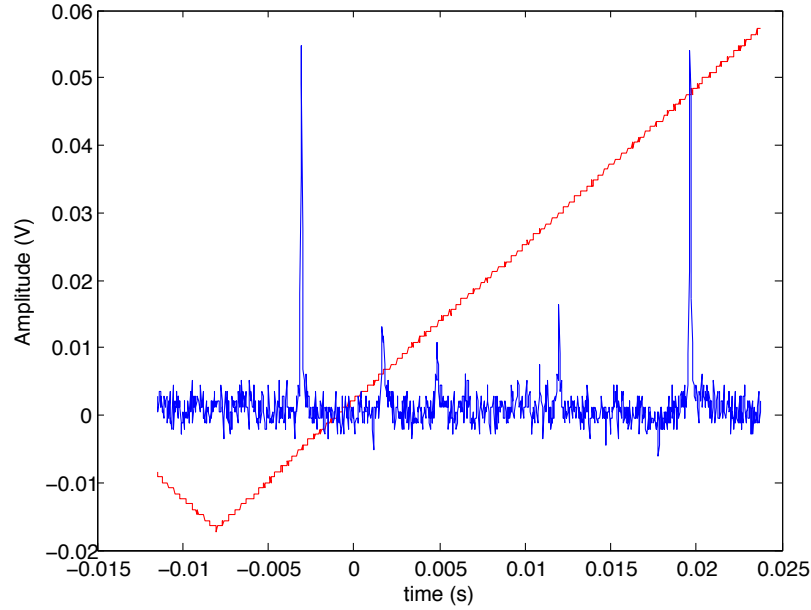


Figure 26: Transmission of the test cavity. In blue is shown the transmitted peaks while in red the voltage ramp on the piezo. As it can be seen a full free spectral range is displayed and the excited modes have a reduced amplitude.

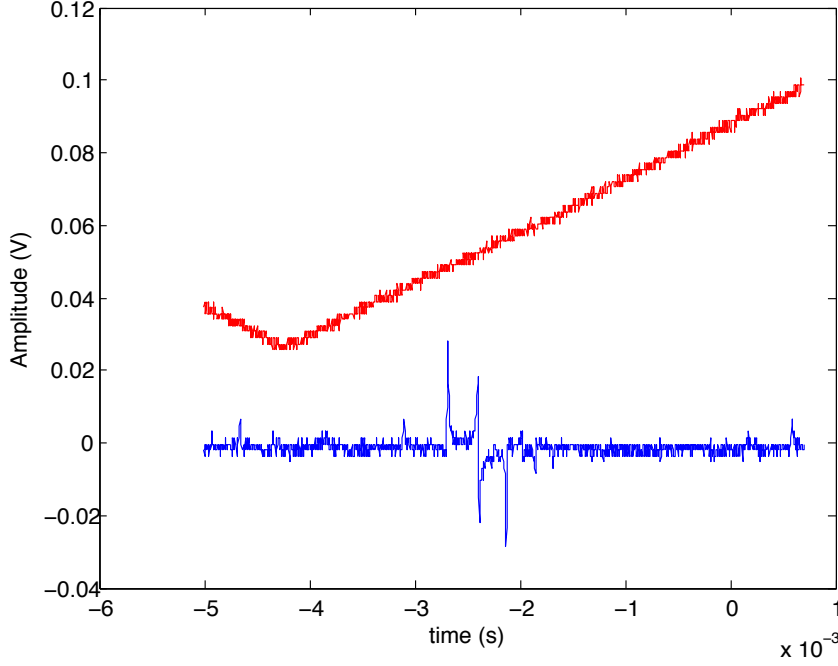


Figure 27: Blue: PDH signal. Red: voltage ramp applied to the cavity piezo. This image was taken using a large modulation power for the sidebands.

Looking at the IF port of the mixer the PDH signal is obtained, see Fig. 27. Such profile was observed while scanning the piezo but, the PDH scheme presented before requires scanning the AOM. The bandwidth of the AOM that we used [26] is limited to 50 MHz and thus doesn't allow to measure the full PDH signal since that EOM frequency of 126 MHz. Therefore it is possible to select the main peak of the signal by changing the voltage applied to the piezo.

The error signal of the main peak is then sent to the E.V.I.L box (Electronically Variable Interactive Lockbox), a digital P.I. controller designed and built by Ludwig de Clercq and Vlad Negnevitsky in our group which controls the frequency of the AOM by changing the voltage of the VCO. With this technique it is possible to lock the laser frequency to the cavity resonance.

Locking has been achieved but only for short periods of time (less than a minute). We think that the reason are mechanical instabilities and vibrations. In particular we think that the flat mirror is more sensitive to vibrations because it is a 1 inch mirror that is mount on a small piezo stack. As a consequence there could be some mechanical stress. Moreover the system is not protected by a box and thus air flow can induce undesired vibrations.

As a side remark, I would like to present a particular behavior of the EVIL output signal that has been obtained while locking the laser, see Fig. (28). As it can be seen there is a periodical repetition of a jump followed by an oscillation. The frequency of this repetition is approximately 300 kHz. We think that this unexpected signal is only dependent on the EVIL; indeed, its shape and frequency can be modified by changing the PI parameters. The jumps can be explained by overflows in the integrator while the oscillations as the EVIL catching up after the jump.

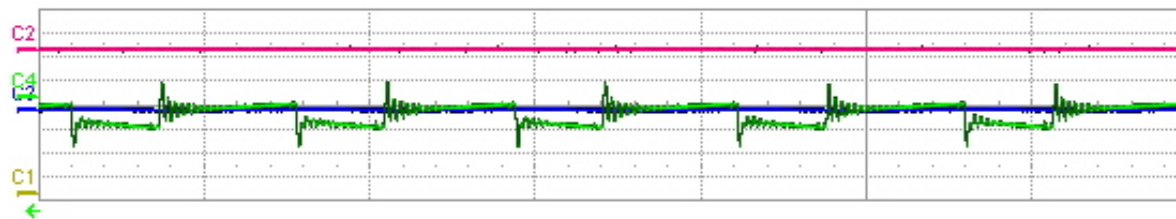


Figure 28: In green the evil output trace. Jumps and oscillations repeats with a frequency of approximately 300 kHz.

A second test we tried to perform was to measure the laser linewidth. From the Verdi data sheet [8], we expect the cavity to have a smaller linewidth than the laser. This means that the width of the transmitted peaks observed while scanning the cavity, will only be related to the laser fluctuation. The measured value is $\Delta\nu \approx 3.5$ MHz which is larger than the theoretical cavity linewidth ($\Delta\nu=1.2$ MHz). Despite this, we are not confident enough to state that the measured value is only dependent on the laser. Indeed, as we already mentioned, this cavity isn't very stable and thus we cannot exclude that its linewidth is exactly the expected one.

From these measurements it is possible to conclude that there is an upper bound for the laser linewidth at 3.5 MHz and that the locking electronics works as expected. Relying on these results we decided to build the high finesse cavity and compare the results.

2.6.2 High finesse cavity

Following the methods and the design described earlier in this chapter we built the high finesse cavity. As a first step we decided to place it in air in order to be able to compensate possible misalignments by tilting the mirror on the polaris mount. In particular we expected to have misalignments on the vertical direction, on the order of $100\ \mu\text{m}$, due to the glue layers which were not taken into account during the design of the mirror holder.

Great efforts were paid to realizing a stable setup and to mode matching the cavity in order to reach the maximum incoupling efficiency. First of all, to get best ellipticity of the beam profile, we used an optical fiber to clean the beam shape that was distorted

by the AOM. Secondly to tune the beam size and curvature we mounted the incoupling lenses on translation stages to fine tune the distances from the cavity mirrors. Moreover, for further stabilization, the cavity was placed into a metallic box to protect it from vibrations, air flow and mechanical stress on the ring holder. This box can be seen in Fig. 29.

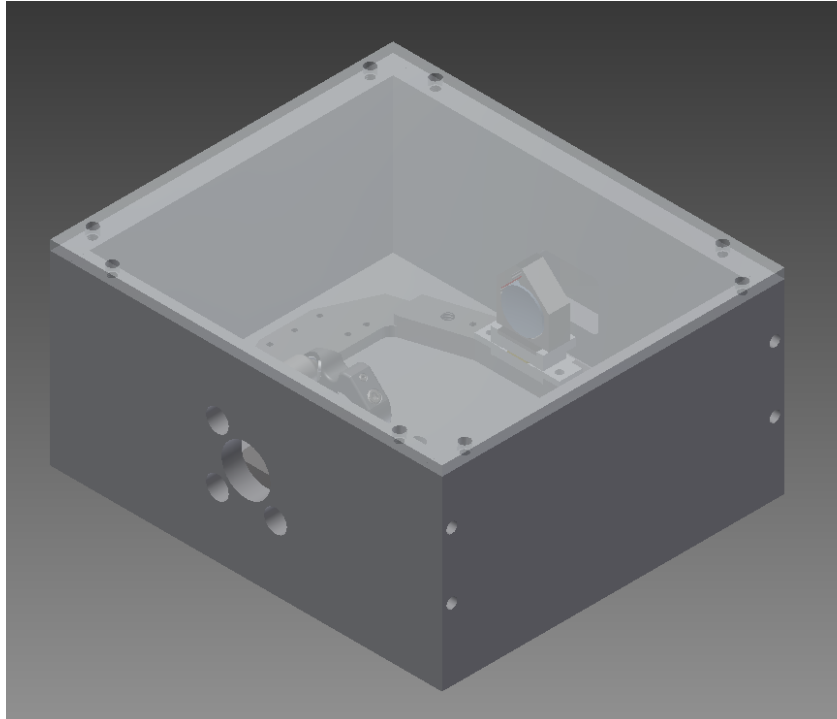


Figure 29: Inventor design of the box used to protect the cavity structure.

To optimize the incoupling, we tried to act on the polaris mount to adjust the orientation of the mirrors. It has to be mentioned that doing this is not so trivial because the screws are very sensitive and don't move fluently. Despite this, we were able to suppress all the higher excited modes of the cavity maximizing the fundamental one. The optimized transmission signal is shown In Fig. 30. This signal was obtained also by optimizing the lens position.

To enhance this result we tried to maximize the incoupling efficiency while locking the laser to the cavity. Fig. 31 shows the PDH signal obtained by scanning the cavity length. Although it has been possible to observe the PDH signal also while scanning the AOM, the locking wasn't stable enough to allow incoupling optimization. We think that the reasons are both fast and slow drifts. The fast ones, could be referred to the laser whose frequency fluctuations are so fast that the PID loop or the VCO response cannot compensate for them. The slow ones, instead, could be given by air flow and vibration on the optical table due to the presence of a cryostat. One possibility which we plan to

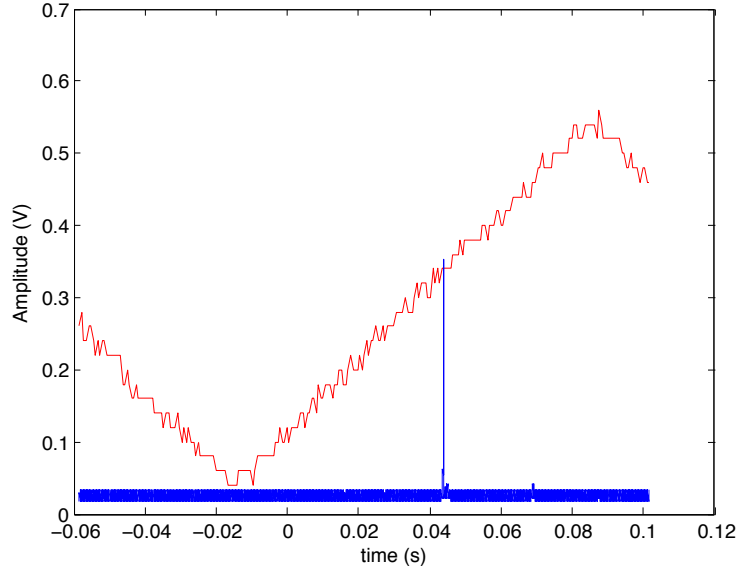


Figure 30: In red piezo ramp. In blue the transmitted peak. As one can see the excited modes are highly suppressed with respect to the fundamental one.

realize in future is to compensate the slow fluctuations using a slow output channel of the EVIL which could act on the cavity piezo. This solution hasn't been implemented yet.

Despite all these efforts it hasn't been possible to go beyond the 3% of incoupling efficiency. To justify this result we explored several possibilities. The first one could be an unbalanced reflectivity of the mirrors due to polarization sensitivity of the coatings. If this is the case, the impedance matching would not be good and the cavity would show increased losses. To test this, a $\lambda/2$ wave plate was placed before the mirrors. We noticed a birefringent effect due to stress on the mirror substrate that was solved by loosening the screws that hold the mirrors in place. Nevertheless to justify a 3% of transmission, it is required that the second mirror have a reflectivity of $R = 0.975$ which is very low compared to the specified one of $R = 0.9998$. This estimation can be obtained by squaring the transmitted electric field amplitude on resonance

$$E_t = \frac{t_1 t_2}{1 - r_1 r_2} , \quad (2.31)$$

where r and t are the refraction and transmission coefficient.

A second possible effect that could induce losses in the cavity is scattering with air particles. To evaluate the losses one can assume air to be composed only of nitrogen molecules, which are the main contributors for green light scattering. The scattering cross-section of this molecule is $5.1 \times 10^{-31} \text{ m}^2$ [33]. This means that at room temperature

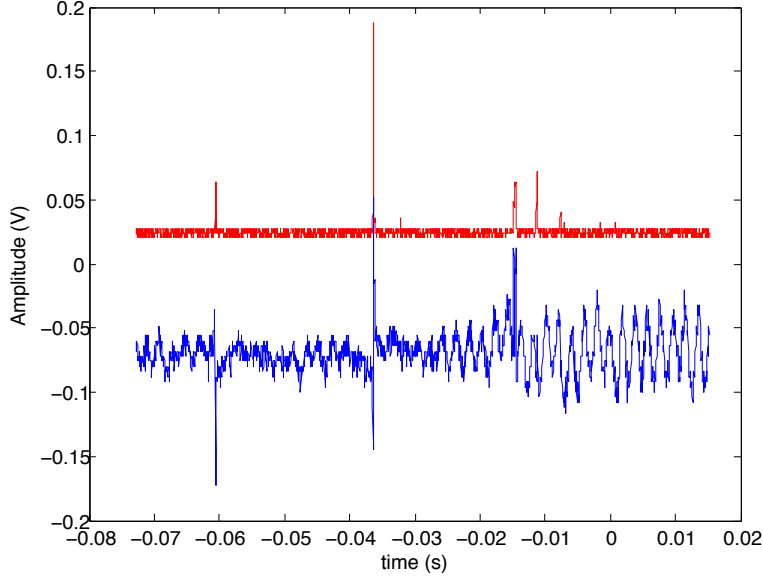


Figure 31: In red cavity transmission. The two sidebands are visible near the central peak. In blue the recorded PDH signal. The blue line was shifted to allow a better view.

and atmospheric pressure (density of air 1.225 kg/m^3) the amount of losses in the 5 cm path of the cavity are of the order of 5×10^{-7} . Therefore it is possible to conclude that scattering cannot influence so much the transmission efficiency.

A third effect that can be considered are diffraction losses due to mirror tiltings [35]. In particular, in case of misalignments, one of the two mirrors has to be tilted for compensation. Therefore, due to the finite aperture of the mirror, diffraction losses can occur.

In considering this effect, we first note that so long as we consider mirrors of infinite radius, the resonator will always be aligned and thus no losses occur, see Fig. 32. As one can see in part b) of Fig. 32 it is possible to recover the fundamental mode around the optical axis. Therefore, as long as the beam spot fully lies on the mirror surface, the diffraction losses would be negligible.

Following the derivation of Hauck *et al.* [35] it is possible to evaluate the loss factor V per resonator bounce by applying a first order perturbation theory for the TEM_{00} mode as

$$V = 1 - \left[1 + 2 \left(\frac{\Delta a}{\omega^2} \right)^2 \right] \exp \left[-2 \left(\frac{a}{\omega} \right)^2 \right], \quad (2.32)$$

where a is the aperture radius, ω is the beam diameter of the TEM_{00} mode at the mirror and Δ is the displacement of the intensity pattern at the mirror.

Assuming the data given in Table 7 ($\omega = 274 \text{ } \mu\text{m}$), the aperture radius of the mirror $a = 6.35 \text{ mm}$ and a total vertical misalignment of $\Delta = 100 \text{ } \mu\text{m}$, it is possible to check

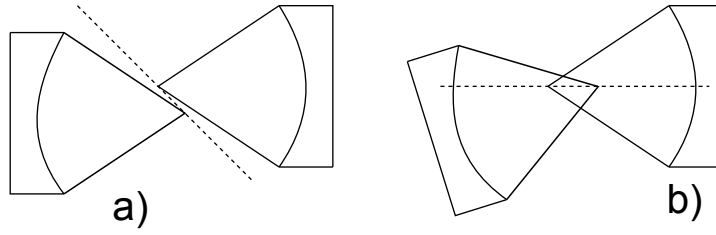


Figure 32: Figure a) shows the initial state where the two mirrors are misaligned in the vertical direction. In this case the optical axis (the line connecting the two centers) doesn't touch the two mirrors. In figure b) the optic axis pass through the center of the second mirror and near the edge of the tilted one. In this case it is possible to recover the fundamental mode.

that $1 - V = 3.6 \times 10^{-460}$ which is absolutely negligible for a finesse of $F \approx 10000$.

From this analysis, and relying on the fact that we were able to observe a nice single mode, we think that the problem isn't the cavity but the laser linewidth which is too broad to allow a better incoupling efficiency. To verify this hypothesis we measured the laser linewidth by measuring the transmitted peak width obtained while scanning the cavity. From this measurement we confirmed a linewidth of approximately 3.5 MHz which agrees with previous estimation done with the test cavity. A second limiting factor is the fact that it not possible to feedback directly to the laser; as a consequence, the compensation for the frequency shifts of the laser is limited by the bandwidth of the VCO.

For this reason and for future experiments with optical trapping we decided to get a new laser which allows better performances. Other goals of this projects are an in vacuum test, to check the system stability after the bake out, and to implement the slow feedback loop acting on the piezo, to allow a better compensation of the slow drifts. The final goal would be to optically trap $^{40}\text{Ca}^+$ using the fiber trap described before.

3 Fiber noise cancellation

In this chapter I will describe experiments in which I built and analyzed the performance of a scheme for fibre phase noise reduction based on feedback. This method is commonly used in apparatus which combine narrow-linewidth lasers with optical communication via optical fibres.

Optical fibers are a flexible tool that allow to separate the experiment from the laser setup. Nevertheless it has been observed [34] that, due to temperature and pressure fluctuation or just mechanical stress on the cable, the laser linewidth can be changed up to some kHz. This phase noise is more evident for longer fibers.

For $^{40}\text{Ca}^+$ qubit manipulation, a laser of 729 nm with a linewidth less than 1 kHz is desirable, thus the fibre phase noise becomes a factor which must be eliminated.

As can be seen from Fig. 33, the full setup is spread in three different zones: on one table is placed the laser, on a second there is the experiment and, for stability reasons, on a third table is placed the ultra high finesse cavity used to reduce the laser linewidth [36].

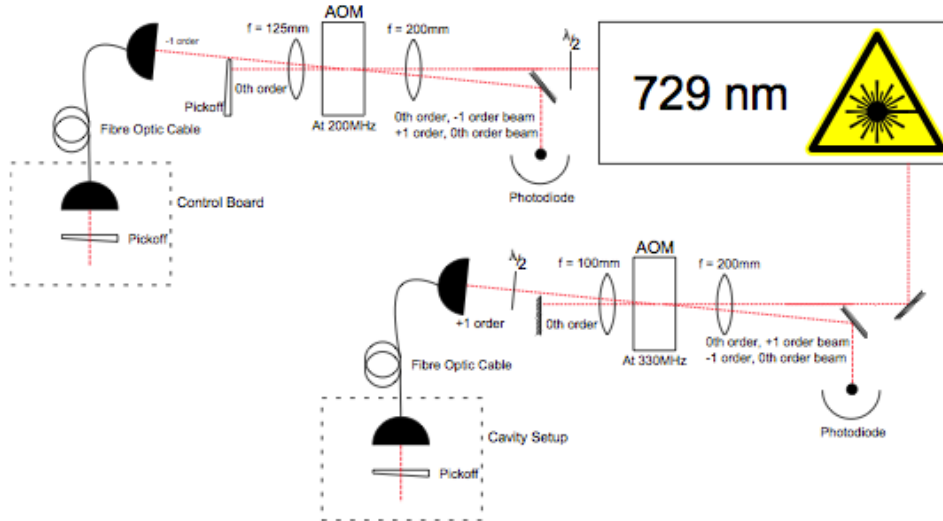


Figure 33: Optical setup for the fiber noise cancellation setup.[36]

The optical connection between these zones is done using 10 m long optical fibers. As a result two different FNC setups are required. A detailed description of the method can be found in K.Fisher master thesis [36] and D.Hume Ph.D thesis [37]. The basic idea is to use the phase shift induced by an AOM (ϕ_{AOM}) to cancel the phase noise introduced by the fibers (ϕ_f). As an example consider the main beam of the 729 nm laser shown in Fig. 33: the laser beam is diffracted into the 0-th and +1-th order by an

AOM which oscillates at a frequency $\nu_{AOM} \approx 200$ MHz. The 0-th order, which is not affected by any phase or frequency shift on the single pass, is retro-reflected through the AOM and diffracts into the -1 order and is sent to a photodiode. This beam will acquire a phase shift ϕ_{AOM} and a frequency shift $-\Delta$. The first order diffracted beam acquires a phase shift $-\phi_{AOM}$ and a frequency shift of $+\Delta$ after the single pass into the AOM. This beam is sent through the optical fiber where it gets partially reflected back using a pickoff. The fiber will imprint a total phase shift of $2\phi_f$ to the light. The back reflected beam pass again through the AOM where the 0-th order is then sent to a photodiode. The two beam going to the photodiode exit the AOM with the same angle and therefore are overlapped. As a consequence it is possible to see a beat note at a frequency

$$\omega_{beat} = 2\Delta - 2\phi_{AOM} + 2\phi_f . \quad (3.1)$$

From this, one can see that the fiber noise can be canceled by locking the AOM phase to the phase shift of the fiber. To apply this method it is required that the phase noise introduced by the fiber is slowly varying compared to the bandwidth of the cancellation system.

3.1 Locking circuit

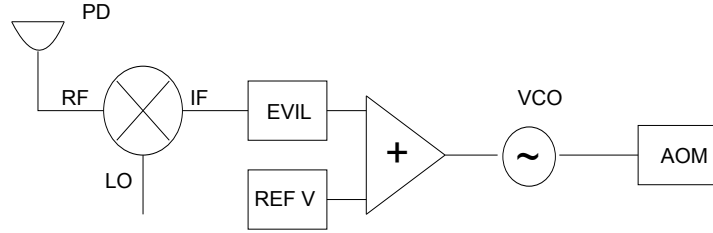


Figure 34: Locking circuit scheme.

In order to lock the the phase of the AOM to the fiber noise phase shift, the feedback loop shown in Fig.34 has been implemented. Although the idea is the same for both the main beam and the slave one, in the following I will focus on the fiber noise cancellation of the main 729 nm beam. In this case, the AOM is driven at ≈ 200 MHz and thus we expect a beat note frequency at $\nu_{beat} \approx 400$ MHz. This optical signal is read using a custom made fast photodiode [38] and converted into an RF signal which is sent to a mini-circuit frequency mixer [39] (model: ZX05-1L+). The RF input is mixed with a DDS frequency at $\nu_{LO} = 400$ MHz sent through the L.O (local oscillator) port. In Fig.35 it is plotted the measured beatnote signal. As one can see the peak is placed onto a pedestal wide ≈ 17 MHz which shows that there is another source of noise that is probably due to the laser T.A. To minimize the conversion losses during the frequency mixing the L.O. signal should be at ≈ 7 dB [39]. In our case the output of the DDS is at 0 dB so, in the future, a stronger L.O signal could improve the full setup.

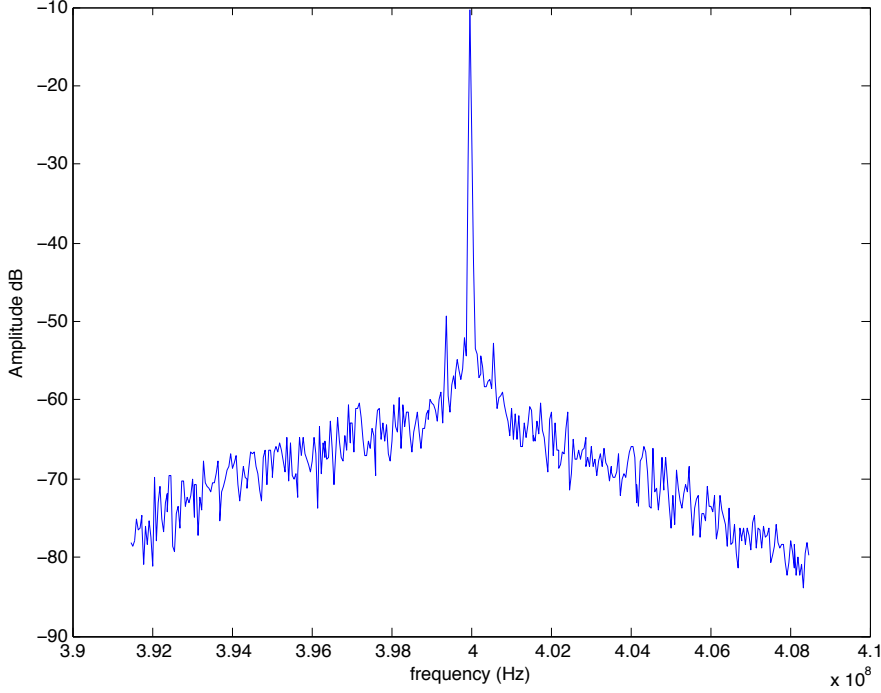


Figure 35: Beatnote plot. The pedestal is wide roughly 17 MHz.

The signal coming from the mixer has two frequency components: one fast at the sum of the two mixed frequency $\nu_{LO} + \nu_{beat}$ and a second DC frequency which is the difference of the two $\nu_{beat} - \nu_{LO}$. The one containing only the information about the phase shifts is the second, thus we select it by passing the signal through a low-pass filter. This DC signal, also called error signal, is then fed into an EVIL box which will output small voltage correction needed to cancel the frequency shift due to the fiber noise. As visible from Fig. 34, this signal is summed with a reference voltage source which sets the VCO [40] (model: Minicircuit jtos-200) frequency at $\nu_{AOM} \approx 200$ MHz. If properly locked the EVIL output should allow noise suppression up to few kHz.

3.1.1 Results

Applying the protocol described above it is possible to lock the system to suppress the noise induced by the optical fiber. In Fig. 36 it is shown the comparison between a locked and an unlocked beat note signal. The unlocked trace was measured using a frequency source and not with the unlocked VCO because the VCO linewidth is on the order of 100 kHz due to electrical and thermal noise. Therefore it is not possible to perform a sensitive measurement. From Fig. 36 one can note that the noise is suppressed sensibly

only up to 1 kHz from the peak with an average suppression around 10 – 15 dBm.

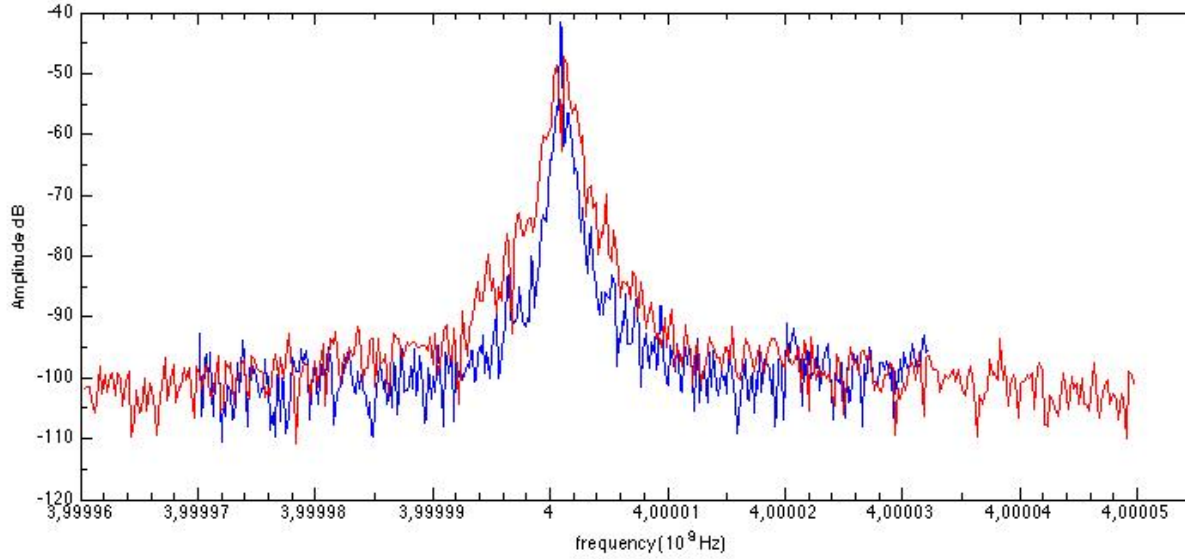


Figure 36: In red the unlocked beatnote, in blue the locked beatnote. The frequency scale is in 10^8 Hz

This result shows that the locking scheme works and that it is possible to partially suppress the fiber noise. Nevertheless its efficiency can be further improved in two way: the first one is by optimizing the fiber incoupling to have a better beat note signal; the second one is reducing the electrical noise by building a single PCB in which all the components are stabilized and isolated from the environment. For example a possible improvement could be stabilizing the reference voltage source and also isolate the VCO from any heating source like resistors.

A final test to check wether this method improves the control of the ion is to measure the effect of FNC on the coherence of the ion. At the moment this is not possible because our current limitation is noise in the magnetic field.

4 Summary and Outlook

This thesis illustrates all the work that has been done to realize a high finesse cavity for optical trapping of ions. I have shown that, compared to $^{40}\text{Ca}^+$ and $^9\text{Be}^+$, $^{25}\text{Mg}^+$ is the better candidate for optical trapping. Its level scheme allows optimal trapping parameters for the states of interest, namely the ground and the P states. From these calculation it has been possible to evaluate the amount of power needed to trap those species using a far detuned laser beam at 532 nm. To get to those values of power (around the kW), we decide to build a high finesse cavity.

After comparing several possibilities, we opt for a near concentric resonator with finesse $F = 10160$, long approximately 5 cm that support a beam waist of 30 μm . The experimental realization of this device shows that it is possible isolate the fundamental mode from the excited ones. Moreover it has been shown that it is possible to partially lock the laser to the cavity using the PDH scheme.

Despite these results it hasn't been possible to obtain an incoupling efficiency beyond 3%. After a detailed analysis we think that this is due to the laser whose linewidth is too broad to allow a better incoupling efficiency. A second limiting factor is the fact that it not possible to feedback directly to the laser; as a consequence, the compensation for the frequency shifts of the laser is limited by the bandwidth of the VCO.

For future experiments we decided to buy a new laser which allows better performances. Other goals of this projects in the short run are an in vacuum tests and the implementation of a slow feedback loop acting on the piezo, to compensate the slow drifts on the piezo. The final goal of this project is to optically trap $^{40}\text{Ca}^+$ using a ion trap fabricated with photonics crystal fibre technology.

This project is a first test for the long term goal which is to build a 3D cavity to create optical lattices for quantum simulation purposes using $^{25}\text{Mg}^+$ ions. The neutral atom community already uses optical lattices, but in that case the coupling between neighbors is given by collision. The great advantage of working with ions, is that the coupling among neighbors sites is given just by the Coulomb interaction and thus it does not require any kind of collisions.

References

- [1] D. J. Wineland, C. Monroe, W. M. Itano, D. Leibfried, B. E. King, and D. M. Meekhof, *Experimental Issues in Coherent Quantum-State Manipulation of Trapped Atomic Ions*, J. Res. Natl. Inst. Stand. Technol. 103, 259 (1998)
- [2] J. I. Cirac and P. Zoller *A scalable quantum computer with ions in an array of microtraps*, Nature 404, 579-581 (6 April 2000)
- [3] D. Kielpinski, C. Monroe and D. J. Wineland *Architecture for a large-scale ion-trap quantum computer*, Nature Vol 417, 13 June 2002
- [4] Ch Schneider, Diego Porras and Tobias Schaetz, *Experimental quantum simulations of many-body physics with trapped ions*, Rep. Prog. Phys. 75 (2012)
- [5] T. Schaetz, A. Friedenauer, H. Schmitz, L. Petersen, S. Kahra, *Towards (scalable) quantum simulations in ion traps*, PQE proceedings, Journal of Modern Optics 54, 2317 (2007)
- [6] A. E. Siegman, *Lasers*, University Science Books.
- [7] *NIST Atomic Spectra Database Lines Form*
http://physics.nist.gov/PhysRefData/ASD/lines_form.html
- [8] *Coherent Verdi V10*
<https://www.coherent.com/products/?1852/Verdi-V-Series>
- [9] W.M. Itano and D.J. Wineland *Precision measurement of the ground-state hyperfine constant of $^{25}\text{Mg}^+$* , Phys. Rev. A Volume 24 Number 3 (1981)
- [10] Rodney Loudon *The quantum theory of light* third edition, Oxford science publication.
- [11] R. Grimm, M. Weidemueller, Y.B. Ovchinnikov *Optical dipole traps for neutral atoms* Advances in Atomic, Molecular and Optical Physics Vol. 42, 95-170 (2000)
- [12] Cohen-Tannoudji and J. Dupont-Roc *Experimental study of zeeman light shifts in weak magnetic field* Phys. Rev. A Vol. 5, 2 (1972)
- [13] N. Manini, *Introduction to the Physics of Matter*, CUSL, Milano, 2013
- [14] Ch. Schneider, M. Enderlein, T. Huber and T. Schaetz, *Optical trapping of an ion*, Nature Photonics, Volume 4, Issue 11, pp. 772-775 (2010).
- [15] http://en.wikipedia.org/wiki/File:Laser_resonator_stability.svg
- [16] Gerhard Kirchmair, *Frequency stabilization of a Titanium-Sapphire laser for precision spectroscopy on Calcium ions*, Diploma Thesis University of Innsbruck.
- [17] Fireder Lindenfelser, *Laser stabilization for quantum information experiments with trapped ions*, Master Thesis ETH Zurich.

- [18] Torben Mueller , *Microscopic Probing and Manipulation of Ultracold Fermions*, Ph.DThesis ETH Zurich.
- [19] L. Lamata, A. Mezzacapo, J. Casanova, E. Solano *Efficient quantum simulation of fermionic and bosonic models in trapped ions*, arXiv:1312.2849 [quant-ph]
- [20] R. Islam, E.E. Edwards, K. Kim, S. Korenblit, C. Noh, H. Carmichael, G.-D. Lin, L.-M. Duan, C.-C. Joseph Wang, J.K. Freericks and C. Monroe *Onset of a quantum phase transition with a trapped ion quantum simulator*
- [21] C. Monroe,¹ R. Raussendorf,² A. Ruthven,² K. R. Brown,³ P. Maunz,^{4,*} L.-M. Duan,⁵ and J. Kim *Large Scale Modular Quantum Computer Architecture with Atomic Memory and Photonic Interconnects*, Phys. Rev. A 89, 022317 (2014).
- [22] R. Blatt and C. F. Roos *Quantum simulations with trapped ions* Nature Physics 8, 277–284 (2012)
- [23] Laseroptik web site <http://www.laseroptik.de>
- [24] Thorlabs <http://www.thorlabs.de/index.cfm>
- [25] Polaris mount
<http://www.thorlabs.de/thorcat/21300/POLARIS-K05-SpecSheet.pdf>
- [26] AAOpto-Electronics. AOM model MT110-A1.5-VIS
<http://www.aaoptoelectronic.com/Documents/MT110-2010.pdf>
- [27] Shear plate actuator Model: CSAP03
<http://www.noliac.com/Default.aspx?ID=7718>
- [28] Thorlabs Piezo stack model AE0203D08F.
<http://www.thorlabs.de/thorproduct.cfm?partnumber=AE0203D08F>
- [29] A.Firedenauer, F.Markert et al. *High power all solid state laser system near 280 nm* Appl. Phys. B 84,371-373 (2006).
- [30] Qubig. — <http://www.qubig.com>
- [31] Drever, Hall et al *Laser phase and frequency stabilization using an optical resonator* PACS:06,07.60,07.65.
- [32] Eric Black *Notes on Pound-Drever-Hall technique* Ligo Project technical note.
<http://www.ligo.caltech.edu/docs/T/T980045-00.pdf>
- [33] M. Snee and W. Ubachs, *Direct measurement of the Rayleigh scattering cross section in various gases*. Journal of Quantitative Spectroscopy and Radiative Transfer, 92, 293 (2005).
- [34] L. Ma, P.Jungner, J. Ye, J.L. Hall, *Delivering the same optical frequency at two places: accurate cancellation of phase noise introduced by an optical fiber or other time-varying path*. Optics letters Vol.19 No21.(1994).

- [35] R.Hauck, H.P.Kortz and H.Weber, *Misalignment sensitivity of optical resonators* Applied Optics, Vol. 19, Issue 4, pp. 598-601 (1980).
- [36] K. Fisher Master thesis *Coherent Control Laser System for the Quantum State Manipulation of Trapped Ions*. TIQI Group ETH Zurich.
- [37] D. Hume Master thesis *Two-Species Ion Arrays for Quantum Logic Spectroscopy and Entanglement Generation*. University of Kentucky, 2002.
- [38] B.Keith Ph.D thesis *A quantum memory qubit in Calcium-43*. University of Oxford, 2007.
- [39] Minicircuit mixer ZX05-1L+ data sheet
<http://217.34.103.131/pdfs/ZX05-1L+.pdf>
- [40] Minicircuit VCO jtos-200 data sheet
<http://217.34.103.131/pdfs/JTOS-200.pdf>

Appendix A: Gaussian beams

One way to analyze free-space propagation of light is through the paraxial wave equation [6]. To derive such result we can start by writing the scalar wave equation for electromagnetic fields

$$[\nabla^2 + k^2] E(x, y, z) = 0 , \quad (4.1)$$

where $E(x, y, z)$ is the phasor amplitude of a field which is sinusoidal in time. Without loosing in generality, we can consider optical beams which propagate primarily in the z direction. Therefore it is convenient to rewrite E as

$$E(x, y, z) = u(x, y, z)e^{-ikz} , \quad (4.2)$$

where the u describes the transverse dependence of the beam. Substituting this last expression in the scalar wave equation one can obtain the description of the transverse field as

$$\frac{\partial^2 u}{\partial x^2} + \frac{\partial^2 u}{\partial y^2} + \frac{\partial^2 u}{\partial z^2} - 2ik \frac{\partial u}{\partial z} = 0 . \quad (4.3)$$

Having already factorized the e^{-jkz} term, the remaining z dependence of u is caused only by diffraction effects; consequently it will always be slow compared to the wavelength, due to the e^{-jkz} term, and also to the transverse variations due to finite width of the beam. For this reason it is convenient to work in the paraxial approximation that consist in neglecting the second derivative of u with respect to z . Therefore we reduce the previous equation to the paraxial wave equation

$$\frac{\partial^2 u}{\partial x^2} + \frac{\partial^2 u}{\partial y^2} - 2jk \frac{\partial u}{\partial z} = 0 . \quad (4.4)$$

The next step in this derivation is to find an analytical expression for a gaussian spherical wave, which is better known as a gaussian beam in free space. To solve this task consider a spherical wave whose origin is in (x_0, y_0, z_0) and has the following form:

$$E(\mathbf{r}, \mathbf{r}_0) = \frac{\exp(-jk|\mathbf{r} - \mathbf{r}_0|)}{|\mathbf{r} - \mathbf{r}_0|} \quad (4.5)$$

Suppose also that there is an observer located at a distance $|z - z_0|$ from the source whose aim is to calculate the transverse amplitude at a point (x, y) . Assuming that the distance $|z - z_0|$ is large compared to the coordinates (x_0, y_0) and (x, y) , the Fresnel approximation to diffraction theory says that Eq.(4.5) can be expanded in $|\mathbf{r} - \mathbf{r}_0|$, where only the first terms are considered. Consequently we are left with an equation that satisfys the paraxial approximation and is given by

$$u(\mathbf{r}, \mathbf{r}_0) = \frac{1}{R(z)} \exp \left[-jk \frac{(x - x_0)^2 + (y - y_0)^2}{2R(z)} \right] , \quad (4.6)$$

where $R(z) = z - z_0$ is the radius of curvature of the spherical wave at position z .

Note that the amplitude of this paraxial spherical wave doesn't fall off with transverse distance. So, written in this way, it cannot be the analytical solution we are looking for. This problem can be overcome in the following way: to start let's consider for simplicity x_0, y_0 being zero, then we can replace the coordinate z_0 with $z_0 - q_0$, where q_0 is an arbitrary complex number. This replacement can be applied to Eq. (4.6) leading to

$$u(x, y, z) = \frac{1}{q(z)} \exp \left[-ik \frac{x^2 + y^2}{2q(z)} \right] , \quad (4.7)$$

where $q(z) = q_0 + z - z_0$ is called complex radius and can be decomposed in the real and imaginary part as follow:

$$\frac{1}{q(z)} = \frac{1}{q_r(z)} - i \frac{1}{q_i(z)} . \quad (4.8)$$

Applying this definition to the above equation leads to

$$u(x, y, z) = \frac{1}{q(z)} \exp \left[-ik \frac{x^2 + y^2}{2q_r(z)} - k \frac{x^2 + y^2}{2q_i(z)} \right] . \quad (4.9)$$

This is exactly the result we wanted to derive. There are two components: the first represents a spherical wave propagating along z with real radius of curvature q_r , while the second takes care of the finite transverse amplitude variation. This last term has the form of a Gaussian profile whose fall off is determined by $q_i(z)$.

Using the standard notation we can replace the real and imaginary parts of the complex radius, $q_r(z)$ and $q_i(z)$ with $R(z)$ and $\pi\omega^2(z)/\lambda$ respectively. Thus we can finally write the equation of gaussian beams as

$$u(x, y, z) = \frac{1}{q(z)} \exp \left[-ik \frac{x^2 + y^2}{2R(z)} - \frac{x^2 + y^2}{\omega^2(z)} \right] . \quad (4.10)$$

As a final remark I would like to emphasize that the propagation for a gaussian beam is entirely determined by

$$q(z) = q_0 + z - z_0 = \frac{1}{R(z)} - j \frac{\lambda}{\pi\omega^2(z)} , \quad (4.11)$$

where the initial value, for $z_0 = 0$, is

$$q_0 = j \frac{\pi\omega_0^2}{\lambda} = jz_R , \quad (4.12)$$

in which we introduced the Rayleigh length z_R as well as the initial beam waist ω_0 . Moreover we can re-elaborate the expression for the size and radius of curvature, to be only functions of the beam waist ω_0 and the wavelength of the light in the medium λ . The result is:

$$\omega(z) = \omega_0 \sqrt{1 + \left(\frac{z}{z_R} \right)^2} \quad (4.13)$$

$$R(z) = z + \frac{z_R^2}{z} . \quad (4.14)$$

5 Acknowledgements

Work in progress